

<https://doi.org/10.1038/s41612-024-00657-7>

Extratropical storms induce carbon outgassing over the Southern Ocean



Magdalena M. Carranza¹✉, Matthew. C. Long², Alejandro Di Luca³, Andrea J. Fassbender⁴, Kenneth S. Johnson⁵, Yui Takeshita⁶, Precious Mongue^{5,6} & Katherine E. Turner⁷

The strength and variability of the Southern Ocean carbon sink is a significant source of uncertainty in the global carbon budget. One barrier to reconciling observations and models is understanding how synoptic weather patterns modulate air-sea carbon exchange. Here, we identify and track storms using atmospheric sea level pressure fields from reanalysis data to assess the role that storms play in driving air-sea CO₂ exchange. We examine the main drivers of CO₂ fluxes under storm forcing and quantify their contribution to Southern Ocean annual air-sea CO₂ fluxes. Our analysis relies on a forced ocean-ice simulation from the Community Earth System Model, as well as CO₂ fluxes estimated from Biogeochemical Argo floats. We find that extratropical storms in the Southern Hemisphere induce CO₂ outgassing, driven by CO₂ disequilibrium. However, this effect is an order of magnitude larger in observations compared to the model and caused by different reasons. Despite large uncertainties in CO₂ fluxes and storm statistics, observations suggest a pivotal role of storms in driving Southern Ocean air-sea CO₂ outgassing that remains to be well represented in climate models, and needs to be further investigated in observations.

The oceans have absorbed about 25% of the anthropogenic carbon over the industrial era¹, and nearly 40% of the oceanic uptake occurs through the Southern Ocean's mixed layer^{2–4}. The remoteness of the Southern Ocean and sparsity of surface CO₂ observations, and differences in climate model representation of upper ocean physics and biogeochemistry in this climatic important region, hinder our ability to predict the fate of emitted carbon in future climate states⁵. State-of-the-art climate models show large uncertainties in seasonal air-sea CO₂ fluxes and biological and physical processes regulating oceanic carbon pathways, leading to discrepancies in the phasing and amplitude of the air-sea CO₂ flux seasonal cycle across models and between models and observations^{6–9}. As a result, discrepancies in the strength of the global ocean carbon sink between models and observations largely stem from the Southern Ocean^{10,11}, where models also predict the largest trends in the ocean's carbon sink¹².

Storm systems inject variability in the upper ocean on scales of a few days, potentially distorting seasonal and annual air-sea CO₂ flux estimates from undersampled or unresolved variability^{13–15}, but many questions remain regarding the direction and magnitude of the CO₂ flux anomaly under storm forcing in the Southern Ocean. Recent observations from

biogeochemical (BGC) Argo floats deployed in the Southern Hemisphere¹⁶ suggest that the Southern Ocean may have released more CO₂ to the atmosphere in the wintertime than previously thought^{17–19}, questioning the strength of the Southern Ocean carbon sink²⁰. Other approaches to estimate air-sea CO₂ fluxes from airborne observations of atmospheric CO₂ gradients²¹, reconstructed estimates of oceanic winter CO₂²², and higher resolution surface observations from a Saildrone mission circumnavigating Antarctica¹⁴ suggest float data may overestimate CO₂ outgassing. Reconciling these different observation-based estimates requires quantifying synoptic variability in the fluxes. High-frequency observations of ocean partial pressure of CO₂, pCO₂, have demonstrated temporal variability on time scales of a few days driven by changes in winds and upwelling regimes^{14,23}. The analysis of hourly wind speed and pCO₂ measurements from the circumpolar Saildrone mission indicates wind speed products and sampling frequencies have the largest impact on air-sea CO₂ flux estimates over the Southern Ocean¹⁴. Undersampling short-term variability introduces uncertainties in air-sea CO₂ mean fluxes (i.e., of 10–25%¹³) that can result in monthly/seasonal mean CO₂ flux biases of +20% that indicate greater outgassing¹⁴, potentially driven by strong storms²⁴. Nicholson et al.²⁴

¹Science Division, Monterey Bay Aquarium Research Institute (MBARI), Moss Landing, CA, US. ²Climate and Global Dynamics Laboratory (CGD), National Center for Atmospheric Research (NCAR), Boulder, CO, US. ³Centre pour l'étude et la simulation du climat à l'échelle régionale, Earth and Atmospheric Department, Université du Québec à Montréal, Montreal, QC, Canada. ⁴Pacific Marine Environmental Laboratory, NOAA/OAR, Seattle, WA, US. ⁵Southern Ocean Carbon Climate Observatory, CSIR, Cape Town, South Africa. ⁶National Institute for Theoretical and Computational Sciences (NITheCS), Cape Town, South Africa.

⁷Department of Geosciences, University of Arizona, Tucson, AZ, US. ✉e-mail: magdalenam@mbari.org

investigated the mechanisms driving synoptic variability in air-sea CO₂ fluxes over the Sub-Antarctic Zone from a summertime Wavglider-Glider mission equipped with turbulence sensors. They found that when strong summer storms induce mixing deeper than the climatological mixed layer depth, they are capable of reversing the air-sea CO₂ flux from ingassing to outgassing; because a mixing layer (i.e., actively turbulent) deeper than the mixed layer (i.e., homogeneous in density) can penetrate into the deep pool of carbon-rich waters.

Observational studies from the most extreme storm events in the tropics and subtropics have revealed a strong local influence on air-sea CO₂ exchange^{25–27}. In the tropics, hurricane-induced vertical mixing typically decreases ocean pCO₂ primarily from surface cooling effects^{25,28,29}. Despite decreases in ocean pCO₂, most studies have found large fluxes of CO₂ from the ocean to the atmosphere, mainly attributed to the increased winds^{25,30} that, through the gas transfer velocity (dependent on wind speed squared), efficiently amplify the magnitude of the CO₂ flux in the direction of the local air-sea CO₂ disequilibrium (i.e., differences in pCO₂ between the ocean and atmosphere, ΔpCO₂). Combining air-sea CO₂ flux observations from a few cyclones with storm statistics, observational studies have projected an increasingly important role of storms in contributing to the summertime and annual air-sea CO₂ outgassing locally (e.g., between 23 and 60% in the China Seas^{26,30}) and globally²⁵. Modeling studies, however, have suggested a weak contribution of tropical cyclones (TCs) to the global air-sea CO₂ flux³¹ because of the integrated effect of opposite CO₂ flux responses to wind forcing depending on pre-existing conditions of ΔpCO₂, compensating effects that occur after the passage of a storm, and the fact that TCs are only active in the summer season. Because TCs can reach hurricane-force winds, TC-induced

changes in upper ocean physical and chemical properties can have considerable magnitude (e.g., cooling of order $\mathcal{O}(1)$ °C, MLD deepening of order $\mathcal{O}(10)$ m, and increases in surface ocean pCO₂ of order $\mathcal{O}(10\text{--}100)$ μatm) while changes in atmospheric pCO₂ appear to be negligible. Thus, most studies have addressed the influence of TCs on global air-sea CO₂ flux, considering cyclone-induced changes in surface ocean pCO₂ and upper ocean physics driven by wind forcing. For any given TC, there can be a variety of responses in ocean pCO₂ (i.e., increases and decreases) that are not only dependent on TC intensity and translation speed but also on the pre-existing upper ocean state, including vertical gradients in carbonate chemistry properties²⁷. In principle, storms will produce changes in ocean physics, with consequences for biology and biogeochemistry, as well as changes in the atmospheric marine boundary, potentially modifying atmospheric pCO₂^{32–34}.

Extratropical cyclones in the Southern Hemisphere (SH) rarely reach hurricane-scale force winds like their tropical counterparts, producing more subtle changes in the upper ocean, but they are much more frequent and active year-round³⁵; showing higher density towards the high latitudes (Supplementary Fig. 1). Here we investigate the role that SH storms play in driving air-sea CO₂ exchange, and estimate their contribution to Southern Ocean annual air-sea CO₂ flux. We take a Lagrangian approach (i.e., tracking storms in atmospheric sea level pressure fields), and construct storm-centric composite anomalies of relevant ocean and atmosphere fields over many storm realizations. We use daily output from a forced ocean-ice integration of the Community Earth System Model (CESM), air-sea CO₂ flux estimates, and other ocean variables derived from BGC Argo floats deployed by the Global Ocean Biogeochemistry (GO-BGC) and the Southern Ocean Carbon and Climate Observations and Modeling (SOCCOM) projects³⁶. Though

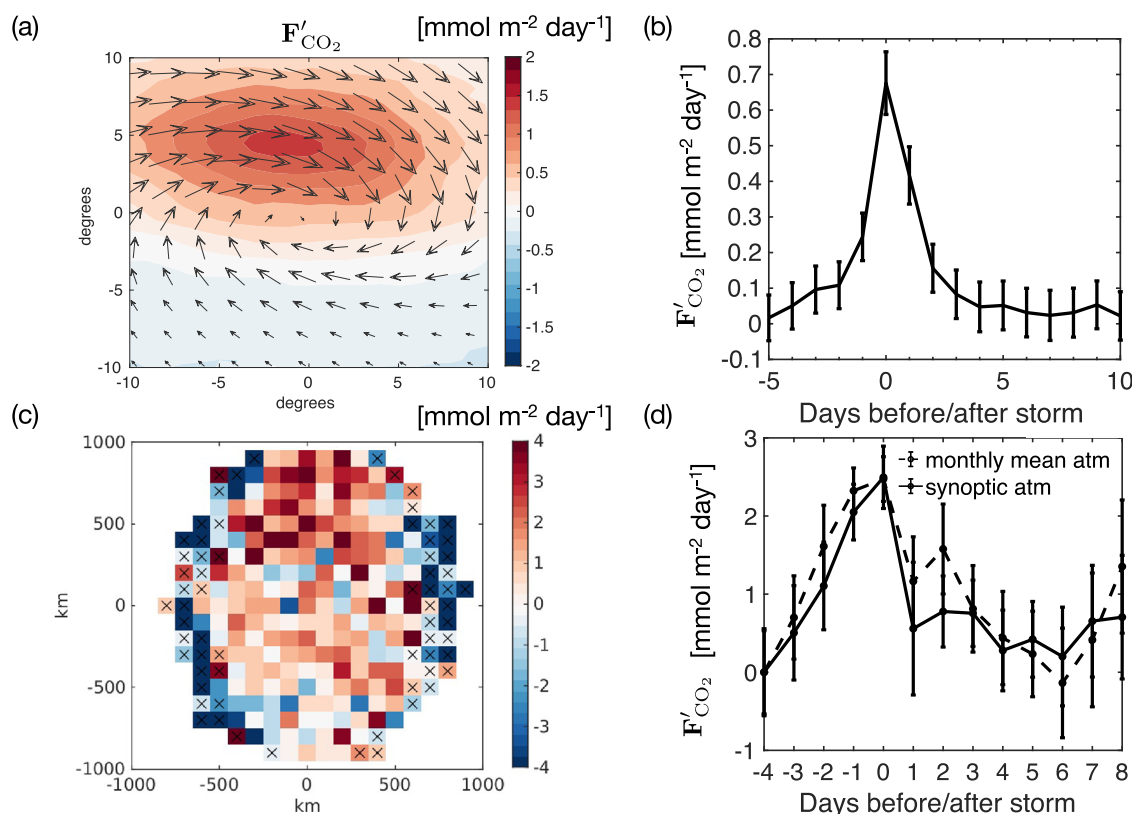


Fig. 1 | Storm composites for air-sea CO₂ flux, F_{CO₂}, anomalies. Annual median CO₂ flux anomalies in storm-centric coordinates for **a** CESM, with averaged vector winds overlaid, and **c** SOCCOM float data. Spatially averaged storm CO₂ fluxes over the equatorward side of storms are 0.65 ± 0.27 mmol m⁻² day⁻¹ for CESM, and 1.45 ± 0.25 mmol m⁻² day⁻¹ for float-derived fluxes. Cross-hatched bins in **c** indicate 100 × 100 km bins with less than 10 float-based estimates. Flux sign convention: positive values imply enhanced outgassing (from the ocean to the atmosphere, red). Time evolution of air-sea CO₂ flux anomalies as a function of time before/after storm

passage for **b** CESM and **d** SOCCOM float data. The dashed line in **d** accounts for synoptic variability in atmospheric pCO₂ and winds, by extracting from ERA5 the averaged atmospheric state at a profile’s location within 24h of a float’s sampling time; whereas the solid line uses the monthly mean pCO₂^{atm} and gas transfer coefficient (at a profile’s location) extracted from the SeaFlux product. Error bars represent the standard error for median values. Note that in **a** and **c** storms are identified from Sea level Pressure (SLP) minima, whereas in **b** and **d**, as an event with CCMP surface winds higher than 10 m s⁻¹ with a persistence of 3 days.

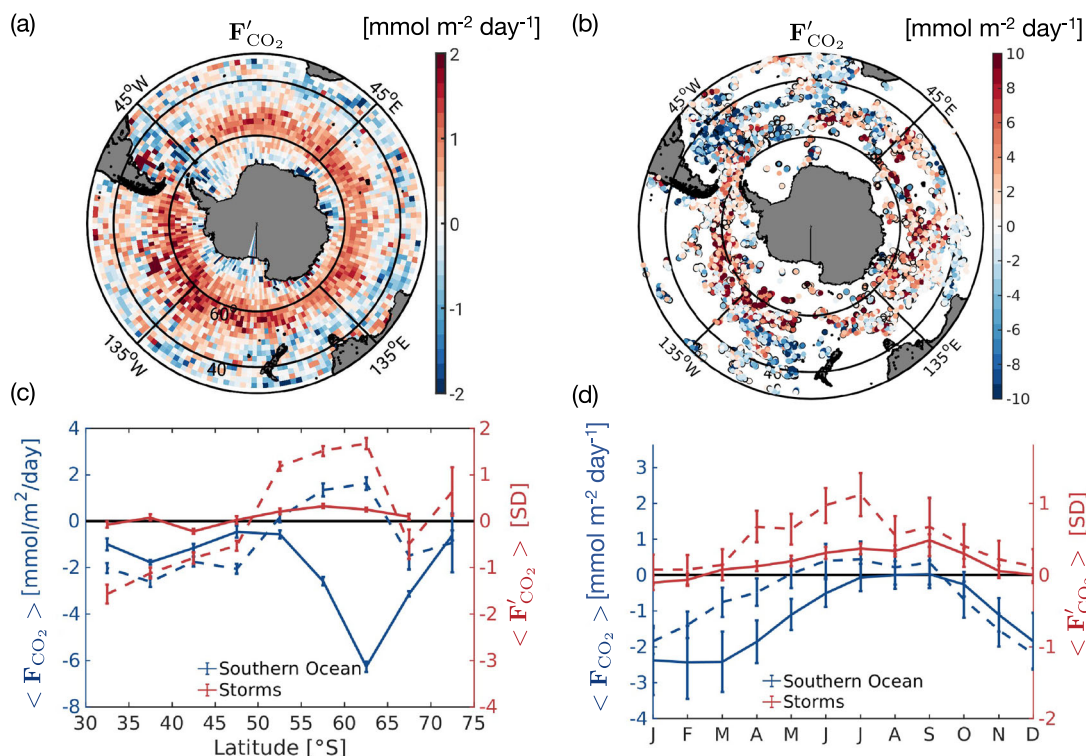


Fig. 2 | Spatial distribution and seasonality of storm anomalies for air-sea CO_2 flux, F'_{CO_2} . **a** Map of storm-induced F'_{CO_2} anomalies in CESM (spatial average considering the top half area, i.e. 0–10° equatorward of storm centers (red in Fig. 1a)). **b** Map of F'_{CO_2} anomalies derived from BGC float profile data. Anomalies of F'_{CO_2} derived from Argo float data are collocated within ERA5 storm centers identified during the period 2014–2022. Float profiles within ~1000 km of a storm center

are circled in black. **c** Zonal and **d** monthly mean standardized storm anomalies of CO_2 flux (red), compared to the median CO_2 flux for the Southern Ocean south of 35° S (blue), from CESM (solid lines) and BGC float data (dashed lines). Error bars represent the standard error for the mean/median. Flux sign convention: positive values imply enhanced outgassing (from the ocean to the atmosphere, red).

each Argo float is programmed to profile every 10 days, floats sample randomly under all weather conditions allowing us to aggregate profiles collected under storms to provide an observational estimate of the mean storm effect on the upper ocean and air-sea CO_2 exchange at the regional scale. We look at storm imprints over the surface ocean following storms, as well as the evolution of anomalies before and after a storm passage. By looking at collocated wind time series within a few days before and after a float profile's sampling time, we can composite BGC Argo float observations in a time before/after storm framework of reference (see Methods). We assess the skill of the ocean component of CESM (at coarse resolution, $1^\circ \times 1^\circ$) in simulating air-sea CO_2 flux changes under storm forcing, by comparing model output with estimates of air-sea CO_2 fluxes derived from BGC Argo floats taking into account potential biases in float data. We estimate how important storms might be in the context of Southern Ocean regional CO_2 exchange, and examine storm-related anomalies in the CO_2 flux and its drivers under storm forcing.

Results

Storms induce CO_2 outgassing

On average storms induce outgassing of CO_2 , as indicated by storm-centric composites of air-sea CO_2 flux anomalies from CESM model output and inferred from BGC Argo float data (Fig. 1). In the model, CO_2 outgassing occurs primarily equatorward of storm's center (Fig. 1a), where winds are stronger and aligned with the mean direction of propagation of cyclonic systems. The spatial pattern in CO_2 outgassing within areas impacted by storms is also discernible in CO_2 flux estimates derived from float data collocated around storms, when referenced to averaged fluxes from profile data outside storms (Fig. 1c). The magnitude of the storm CO_2 outgassing anomaly (i.e., spatially averaged CO_2 flux anomalies over the equatorward side of a storm center) is larger in float data ($\sim 1.45 \pm 0.25\ mmol\ m^{-2}\ day^{-1}$ or $\sim 0.53 \pm 0.09\ mol\ m^{-2}\ yr^{-1}$), albeit somewhat noisier spatially relative to

storm centers, compared to CESM ($\sim 0.65\ mmol\ m^{-2}\ day^{-1}$ or $\sim 0.24\ mol\ m^{-2}\ yr^{-1}$), by at least a factor of 2 (Fig. 1, and Supplementary Fig. 2). Summertime CO_2 flux estimates from a Waveglider mission in the Sub-Antarctic Zone of the Southern Ocean also indicate that strong storms can induce CO_2 outgassing of order $1\ mmol\ m^{-2}\ day^{-1}$ ²⁴. The greater correspondence in the magnitude of the storm CO_2 flux anomalies between Argo floats and Waveglider observations suggests deficiencies in the model in its representation of relevant oceanic processes associated to storms may lead to weaker storm CO_2 outgassing anomalies in the model.

Notably, storm CO_2 outgassing maximizes at day zero (i.e., within a day of the passage of a storm) both in the model and in float-based CO_2 flux estimates (Fig. 1b and d). We will show that anomalies in the gas transfer velocity and the ΔpCO_2 , which determine the air-sea CO_2 flux (see Methods), show the same phasing as the CO_2 flux anomaly, maximizing at day zero. Although changes in oceanic conditions that are conducive to CO_2 outgassing are detectable in the model (e.g., enhanced surface dissolved inorganic carbon), these lag the CO_2 outgassing anomaly by at least 3 days, indicating the oceanic response is not the main driver of CO_2 outgassing in the model.

Storm-induced CO_2 outgassing occurs over a broad latitudinal band in the model, mostly in the Sub-Antarctic Zone, and stronger outgassing is detected over the Pacific sector of the Southern Ocean (Fig. 2a). In float observations, CO_2 outgassing anomalies (relative to the averaged CO_2 flux for float profiles outside storms), is confined to higher latitudes compared to the model, but show the zonal asymmetry in CO_2 fluxes previously identified in float-based CO_2 flux estimates³⁷. There is a tendency for negative CO_2 flux anomalies, indicating uptake, in the southwestern South Atlantic and towards subtropical latitudes, both in the model and observations (Fig. 2a, b). Though float-based estimates are more sparse, there is general agreement in the spatial distribution of storm CO_2 flux anomalies

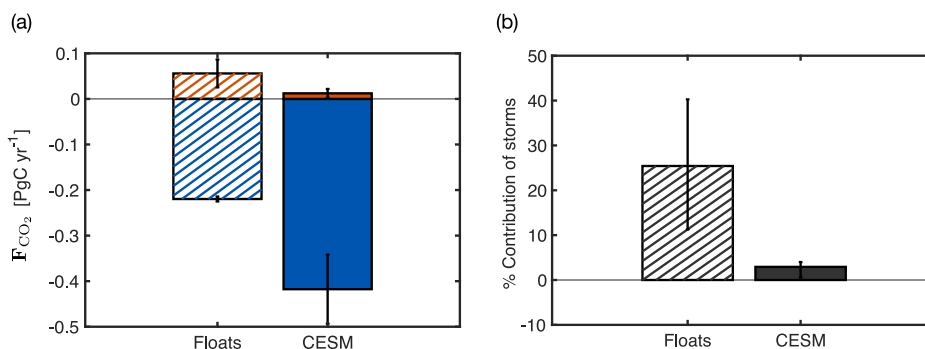


Fig. 3 | Storm’s contribution to Southern Ocean’s annual air-sea CO₂ exchange. **a** Annual storm-induced CO₂ outgassing (red) compared to the annual CO₂ uptake for the Southern Ocean (blue), and **b** percent contribution of storms (i.e. ratio between red and blue bars in **a**), for CESM (solid bar) and BGC float data (dashed bar). Error bars in **a** are maximum and minimum values expected given the standard error in the CO₂ flux estimate (i.e., +1.45 ± 0.25 mmol m⁻² day⁻¹, median storm imprint in Fig. 1c), for an average area of impact (i.e. half the area of a disk of 700 km

radius), the minimum/maximum number of storms identified per year in each forcing field, and storm duration of 3 ± 0.5 days (see Supplementary Note 1). For float-based estimates, we use the average number of storms detected in ERA5 annually, whereas for CESM estimates we use the average number of storms identified in the CORE-IAF forcing. Error bars in **b** are derived from propagation of error of the ratio.

(Fig. 2a, b). The change in sign in the storm CO₂ flux response between the subtropics and sub-Antarctic regions, evident in the zonally averaged CO₂ fluxes derived from float observations (dashed red line in Fig. 2c) suggests an influence of the latitudinal differences in drivers of ocean pCO₂ and background seasonality (see Supplementary Note 5, and review by Gray²⁰). However, in the model, the storm CO₂ ingassing in the subtropics is not statistically significant in a zonal average sense (Fig. 2c), and we will show that ocean pCO₂ is not the main driver of the CO₂ flux anomalies in the model.

Storm CO₂ flux anomalies indicate that, on average, storms induce outgassing nearly year-round but it is stronger in the wintertime (Fig. 2d), particularly in float data. In CESM, storm CO₂ wintertime outgassing is on average ~1.2 mmol m⁻² day⁻¹ and only slightly more persistent than in the annual median (3–4 days, Supplementary Fig. 6c, d and Fig. 1b). Wintertime CO₂ outgassing in CESM is comparable in magnitude to the annual median storm CO₂ flux imprint in float data (Fig. 1c). However, float data also indicate much stronger CO₂ outgassing than the model in the wintertime (i.e., 2.42 mmol m⁻² day⁻¹). Because the magnitude of the storm CO₂ flux anomaly can have different implications depending on the local background seasonal variability in the CO₂ fluxes, in Fig. 2d, we show averaged standardized storm anomalies (i.e., normalizing anomalies by the standard deviation of the seasonal cycle at each storm/profile location before averaging, see Methods and Supplementary Fig. 3). Thus, while the storm CO₂ flux anomaly in the model is on average only ~15% relative to the local variability of the seasonal cycle, float data indicate annual mean storm CO₂ flux anomalies that are ~48% of the variability in the seasonal cycle, but about 100% in the wintertime (July, red dashed line in Fig. 2d). Nonetheless, individual storms can induce CO₂ ingassing particularly in the summer, as indicated by mean storm CO₂ flux anomalies that are near zero (red lines in Fig. 2d). Summertime storms inducing CO₂ ingassing in the model is consistent with 95% of pre-storm conditions in which waters are undersaturated with respect to CO₂ (i.e., CO₂ flux into the ocean, see Supplementary Fig. 5 and 6), in which case the storm CO₂ flux anomaly come from enhancement of the existing CO₂ flux direction through an increased gas transfer velocity (Supplementary Fig. 6d). However, we will show that in the model storm CO₂ flux anomalies drive outgassing most of the time, through changes in the CO₂ disequilibrium between the ocean and atmosphere (i.e., ΔpCO₂).

Storms’ contribution to the Southern Ocean’s annual air-sea CO₂ flux

Extratropical cyclones in the SH clearly have an influence on air-sea CO₂ exchange. Observations suggest that the magnitude of the CO₂ outgassing anomalies is comparable to the local seasonal variability, particularly in the 50–65 °S latitudinal band and in the wintertime (Fig. 2c, d, red dashed lines).

But how important are these anomalies relative to the annual air-sea CO₂ uptake? Here, we compare the magnitude of the storm CO₂ flux anomalies with the annual Southern Ocean flux, and the amplitude of its seasonal cycle, and estimate the contribution of storms to the annual air-sea CO₂ exchange from storm statistics.

The CO₂ flux anomaly over regions impacted by storms in CESM is on average ~+ 0.65 mmol m⁻² day⁻¹ (Fig. 1a). The Southern Ocean’s annual air-sea CO₂ flux (i.e., median across the entire Southern Ocean south of 35°S) in CESM is -1.27 mmol m⁻² day⁻¹ (i.e., ~-0.46 mol m⁻² yr⁻¹), indicating net uptake (Fig. 2d, blue line). Thus, storm CO₂ outgassing represents ~51% of the magnitude of the annual Southern Ocean CO₂ flux in the model, based on the 6-year climatology (range of ~12–53%, from year-to-year variability). For float data, the seasonal cycle of the Southern Ocean’s CO₂ flux shows slight outgassing in the winter season (dashed blue line, Fig. 2d), consistent with previous findings of outgassing particularly towards the high latitudes of the Southern Ocean^{18,19}. Thus, the annual median CO₂ flux across the Southern Ocean in float-based observations is reduced, compared to the model, to -0.58 mmol m⁻² day⁻¹. As a result, the storm CO₂ flux estimate of +1.45 mmol m⁻² day⁻¹ from float data (Fig. 1c), represents 250% of the annual median CO₂ flux derived from observations.

To get a sense of the magnitude of storm CO₂ flux anomalies throughout the seasons, in Fig. 2d, we showed monthly mean standardized storm anomalies (in red). Here we compare the average storm CO₂ outgassing anomaly (Fig. 1a, c) with the amplitude of the seasonal cycle for the median Southern Ocean flux (Fig. 2d, in blue). The median storm CO₂ flux anomaly is more than twice as high in float data compared to CESM (+1.45 mmol m⁻² day⁻¹ vs. +0.65 mmol m⁻² day⁻¹). The amplitude of the seasonal cycle of CO₂ flux for the Southern Ocean agrees relatively well between float estimates and the model (2.63 mmol m⁻² day⁻¹ for floats, and 2.46 mmol m⁻² day⁻¹ in CESM), when considering the median as the metric for averaging, both in the model and observations (in space and time). This comparison indicates storm CO₂ flux anomalies are 55.1% of the annual amplitude based on float data, and 26.4% in the model. We also estimate the contribution of storm CO₂ flux to the annual carbon uptake for the Southern Ocean (Fig. 3), considering the average number of storms per year, N_{storms}, area impacted by storms, A_{storm}, and storm’s duration, τ_{storm}, as follows:

$$F_{CO_2}^{storms} = F'_{storm} \times A_{storm} \times N_{storms} \times \tau_{storm}; \tag{1}$$

where F'_{storm} is the median CO₂ flux anomaly around storms, A_{storm} is estimated as half the area of a disk of 700 ± 50 km radius (see Supplementary Fig. 1), and τ_{storm} = 3 ± 0.5 days (see Carranza et al.³⁵). For the total Southern Ocean carbon uptake, we multiply the median CO₂ flux for all grid cells or float profiles south of 35°S by the Southern Ocean area, as estimated from

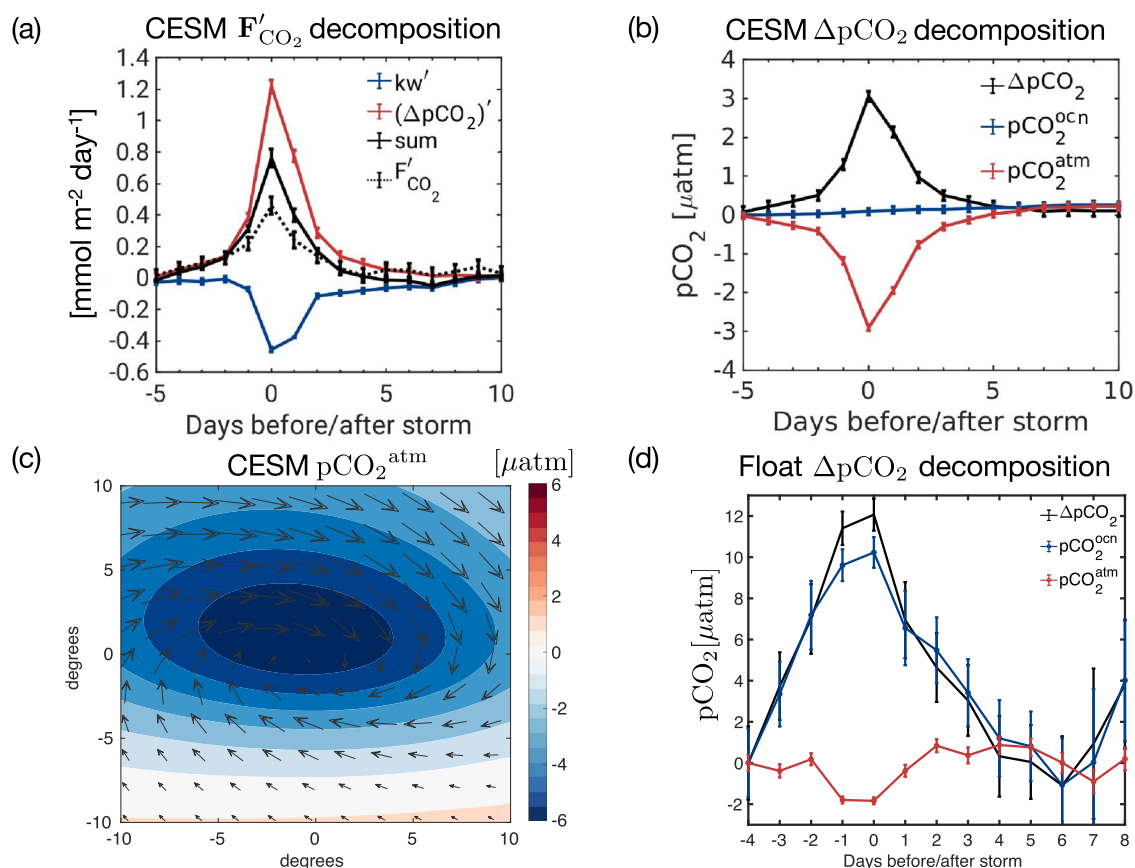


Fig. 4 | CO₂ flux anomaly decomposition analysis for areas impacted by storms. **a** Time evolution of anomalies in $\Delta p\text{CO}_2$ (red), the gas transfer velocity term k'_w (blue), and the reconstruction (black), compared to the total CO₂ flux anomaly (dashed black), see Methods. **b** Time evolution of anomalies of $\Delta p\text{CO}_2$, $p\text{CO}_2^{\text{ocn}}$, and $p\text{CO}_2^{\text{atm}}$. The spatial imprint of storms in **c** anomalies of $p\text{CO}_2^{\text{atm}}$ in storm-centric

coordinates. **a–c** for CESM and storms tracked in CORE-IAF forcing for the period 2009–2014. **d** Analogous to **b** for anomalies derived from BGC Argo float data and collocated ERA5 atmospheric pressure, identifying a storm event as a period of 3 days with averaged winds above 10 m s⁻¹.

the CESM model grid (i.e., $A_{SO} = 91.800.000 \text{ km}^2$, south of 35°S). Even though some storm characteristics can be uncertain on a storm-by-storm basis (e.g., area of impact of a storm due to the asymmetry of extratropical systems), we can make reasonable assumptions about average storm area, duration, and CO₂ flux anomaly from storm statistics (Supplementary Table 1), and account for variability in storm characteristics in upper and lower bound estimates to construct error bars in Fig. 3. We find that the storms contribution to the Southern Ocean’s air-sea CO₂ exchange from storm statistics (i.e., eq. (1)) is $\sim +0.057 \text{ PgC yr}^{-1}$ for float-based estimates, and $\sim +0.016 \text{ PgC yr}^{-1}$ in CESM, which compared to the total Southern Ocean carbon uptake implies an averaged contribution of $\sim 26\%$ in float observations, and $<5\%$ in CESM. Despite large errors due to uncertainties in storm statistics and fluxes, the storm contribution to outgassing from float-derived fluxes is at least 10%, but could be as large as $\sim 40\%$ (Fig. 3), and thus, observations suggest at least an order of magnitude higher storm CO₂ outgassing than in CESM. The discrepancy in the total annual exchange of CO₂ accounted by storms between the model and observations is even more pronounced when considering mean fluxes as opposed to median fluxes (Supplementary Figs. 3 and 4), which suggests an important role of storms in extreme CO₂ outgassing events.

Overall, our analysis indicates a larger contribution of storm CO₂ outgassing in float-based estimates, relative to CESM. Given the outsized contribution of storms to air-sea CO₂ exchange suggested from observations, in the next section, we explore the drivers of the CO₂ flux anomaly under storm forcing. We will show that the discrepancy in the storm CO₂ flux response essentially comes from negligible storm $p\text{CO}_2^{\text{ocn}}$ anomalies in the model, compared to float-based estimates.

What drives storm CO₂ outgassing?

To understand the drivers of the storm CO₂ flux anomalies, we decompose the flux anomaly into contributions from anomalies in $\Delta p\text{CO}_2$ and anomalies induced by changes in the gas transfer and solubility coefficients (i.e., $k'_w = (\kappa\alpha(1 - f_{\text{ice}}))'$, see Methods and Fig. 4).

The storm CO₂ flux anomaly decomposition shows that changes in the gas transfer coefficient (e.g., expected from increased winds or cooler sea surface temperatures, SSTs) on average act to increase CO₂ uptake (Fig. 4a and Supplementary Fig. 7, blue line). This is consistent with high winds enhancing the CO₂ flux in the direction of the flux for pre-storm conditions³¹, as the sign of $\Delta p\text{CO}_2$ (in the model and observations) indicates a CO₂ flux into the ocean most of the time (Supplementary Note 6). In the model, $\Delta p\text{CO}_2$ five days prior to a storm’s passage indicates ingassing conditions $\sim 75\%$ of the time, and outgassing conditions only $\sim 25\%$ of the time (from year-round data), with a larger fraction of pre-storm CO₂ ingassing conditions in the summer and fall (Supplementary Fig. 6). Because in the model wintertime median CO₂ fluxes are weak (Fig. 2d), and there are more storms encountering CO₂ outgassing conditions ($\sim 40\%$, Supplementary Note 6), one might expect the gas transfer velocity effect to change sign according to the season. Indeed in the model, there is seasonality in the sign and magnitude of the wind effect with slightly positive k'_w in winter (i.e. $\sim 0.1 \text{ mmol m}^{-2} \text{ day}^{-1}$, Supplementary Fig. 6c) indicating high winds enhance wintertime CO₂ outgassing. On the other hand, larger negative k'_w in summer results in stronger CO₂ ingassing due to the wind effect that overcompensates the $\Delta p\text{CO}_2$ effect, to produce median storm CO₂ ingassing anomalies in the summer (i.e., $\sim -0.8 \text{ mmol m}^{-2} \text{ day}^{-1}$, Supplementary Fig. 6d).

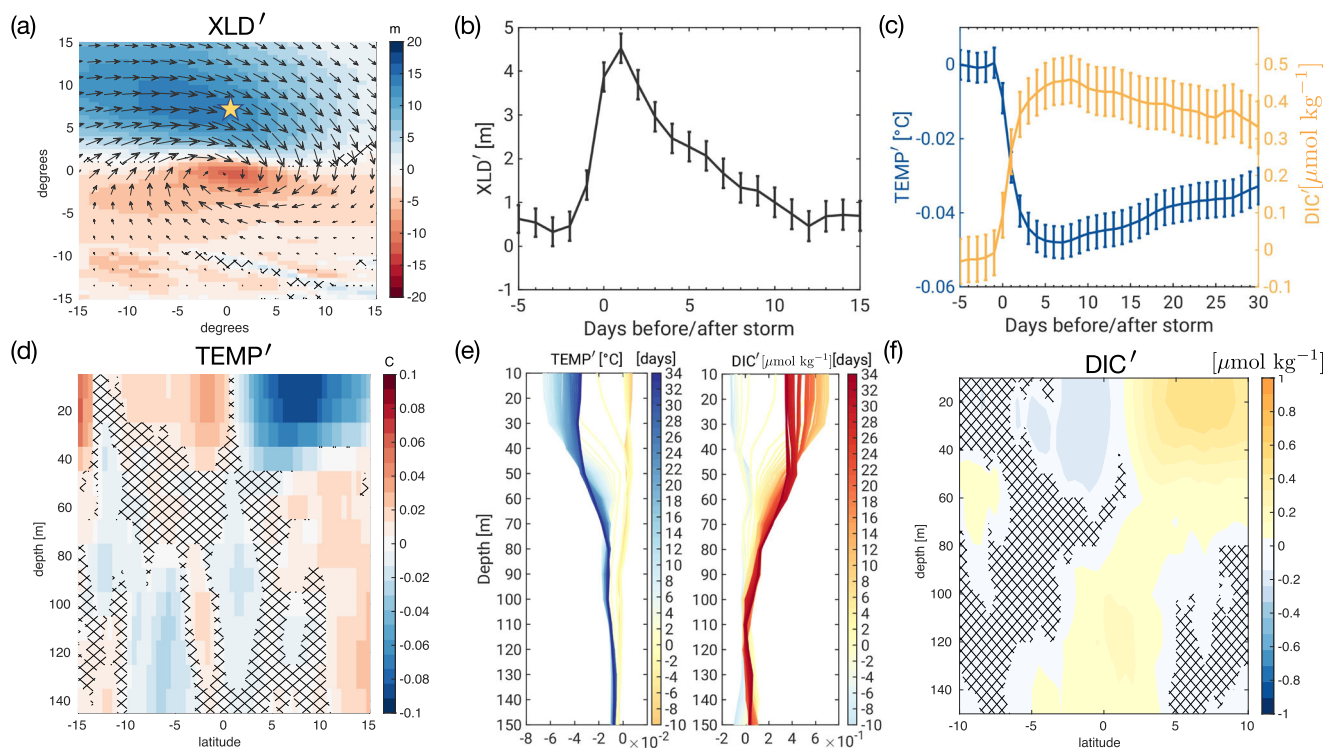


Fig. 5 | Spatial imprints and time evolution of storm-induced anomalies in CESM. **a** Spatial imprint of averaged mixing-layer depth (XLD) anomalies at $t = 0$, in storm-centric coordinates. **b** XLD, **c** sea surface temperature (SST) and surface dissolved inorganic carbon (DIC) spatially averaged anomalies (i.e. top 10m), within proximity of storm centers (i.e., equatorward side of storms) in a before/after storm framework. Vertical structure (depth vs. degrees latitude relative to storm centers for **d** temperature at $t = 3$ days, and **f** DIC at $t = 7$ days, when storm anomalies maximize.

Cross-hatched areas are non-significant at the 90% level, from bootstrap sampling (i.e. $N = 100$, and a standard error estimated from the standard deviation of the distributions of medians). **e** Mean temperature and DIC anomaly profiles, 7.5° north of storm centers (yellow star in **a**), color-coded by time relative to the passage of a storm (in days, see colorbar). CESM model output for the 2009–2014 period (i.e., ~ 4000 storms).

However, except for summertime conditions, the largest contribution to the CO_2 flux anomaly that also explains the sign of the air-sea CO_2 flux anomaly associated with storms comes from anomalies in $\Delta p\text{CO}_2$, both in the model (Fig. 4a, red) and observations (Supplementary Fig. 7, red). Further partitioning the $\Delta p\text{CO}_2$ anomalies into contributions from oceanic $p\text{CO}_2$, $p\text{CO}_2^{\text{ocn}}$, and atmospheric $p\text{CO}_2$, $p\text{CO}_2^{\text{atm}}$, anomalies (Fig. 4b) indicates that, in the model, it is the drop in $p\text{CO}_2^{\text{atm}}$ that drives the change in $\Delta p\text{CO}_2$. In this forced-ocean simulation, the mixing ratio of CO_2 in the air is globally uniform; thus, the change in $p\text{CO}_2^{\text{atm}}$ is entirely driven by the drop in atmospheric pressure associated with the storm (Fig. 4c). As indicated in Fig. 4b, the storm-induced anomalies in $p\text{CO}_2^{\text{ocn}}$ in this configuration of CESM are negligible compared to the anomalies in $p\text{CO}_2^{\text{atm}}$.

An analogous $\Delta p\text{CO}_2$ anomaly decomposition into oceanic and atmospheric $p\text{CO}_2$ anomalies can be performed for float observations, and it indicates a larger role of $p\text{CO}_2^{\text{ocn}}$ than suggested by the model (Fig. 4d). In the time-domain framework, we detect storm anomalies in $\Delta p\text{CO}_2$ of nearly $12 \mu\text{atm}$ (Fig. 4d, black line), over three fold larger than the average storm-induced $\Delta p\text{CO}_2$ anomalies detected in the model (i.e., $< 3 \mu\text{atm}$, Fig. 4b). Quantitative differences in the magnitude of the $\Delta p\text{CO}_2$ anomalies between the model and observations are expected from differences in the analysis periods considered and the fact that not all storms will have been sampled by floats across the entire area of a storms' impact, as well as differences in the baselines to calculate storm anomalies (see Methods, and Supplementary Fig. 2). However, because it is on average the $\Delta p\text{CO}_2$ that drives the CO_2 flux anomaly, and $p\text{CO}_2^{\text{atm}}$ increases at a higher rate than $p\text{CO}_2^{\text{ocn}}$, extrapolating the data analysis to coincident time periods would result in larger discrepancies (based on a trend analysis of storm anomalies, not shown). Most notably, $p\text{CO}_2^{\text{ocn}}$ in float data indicates an increase relative to pre-storm conditions of $\sim 10 \mu\text{atm}$, which combined with the drop in $p\text{CO}_2^{\text{atm}}$, acts to

enhance the $\Delta p\text{CO}_2$ anomaly and, as a result, the storm air-sea CO_2 outgassing inferred from float data. This demonstrates that, despite overall good agreement in ocean $p\text{CO}_2$ between the model and observations on seasonal scales (Supplementary Note 5), the storm CO_2 outgassing anomaly is driven by different mechanisms in the model and observations.

Next, we will show that, even though changes in upper ocean conditions are detectable in the model, which are consistent with modifications in ocean circulation and mixing under storm forcing (e.g., SST cooling expected from enhanced mixing, Fig. 5), these are out of phase (lagging by at least 3-4 days) and therefore cannot explain the strong CO_2 outgassing anomaly within a day of a storm's passage (at zero lag) in the model.

Storm's influence on upper ocean physics and dissolved inorganic carbon

Changes in upper ocean physics in the model are consistent with high-winds expected from storm forcing (Fig. 5), showing deeper mixing layers on the equatorward side of storms (Fig. 5a) where wind stress is enhanced due to the alignment between the wind perturbation from the storm and its translation speed^{38–40}. Mixing-layer depth (XLD) anomalies in the model are of order $\mathcal{O}(1-10)$ m, and reach their deepest expression a day after a storm's passage (Fig. 5b). Both the XLD and the mixed-layer depth (MLD, not shown) deepen by similar magnitudes after the passage of a storm in the model. Deep mixing is in agreement with surface cooling of a sizable magnitude ($\mathcal{O}(0.1)$ °C, Fig. 5c–e) and small but detectable changes in surface dissolved inorganic carbon (DIC, $< 1 \mu\text{mol kg}^{-1}$, Fig. 5c, e, f). The vertical structure of temperature and DIC anomalies for the top 150 m indicates that the cooling and DIC enhancement occur over the top 50–70m of the water column (Fig. 5e). But, while the XLD deepening maximizes a day after the passage of a storm, the SST and surface DIC response

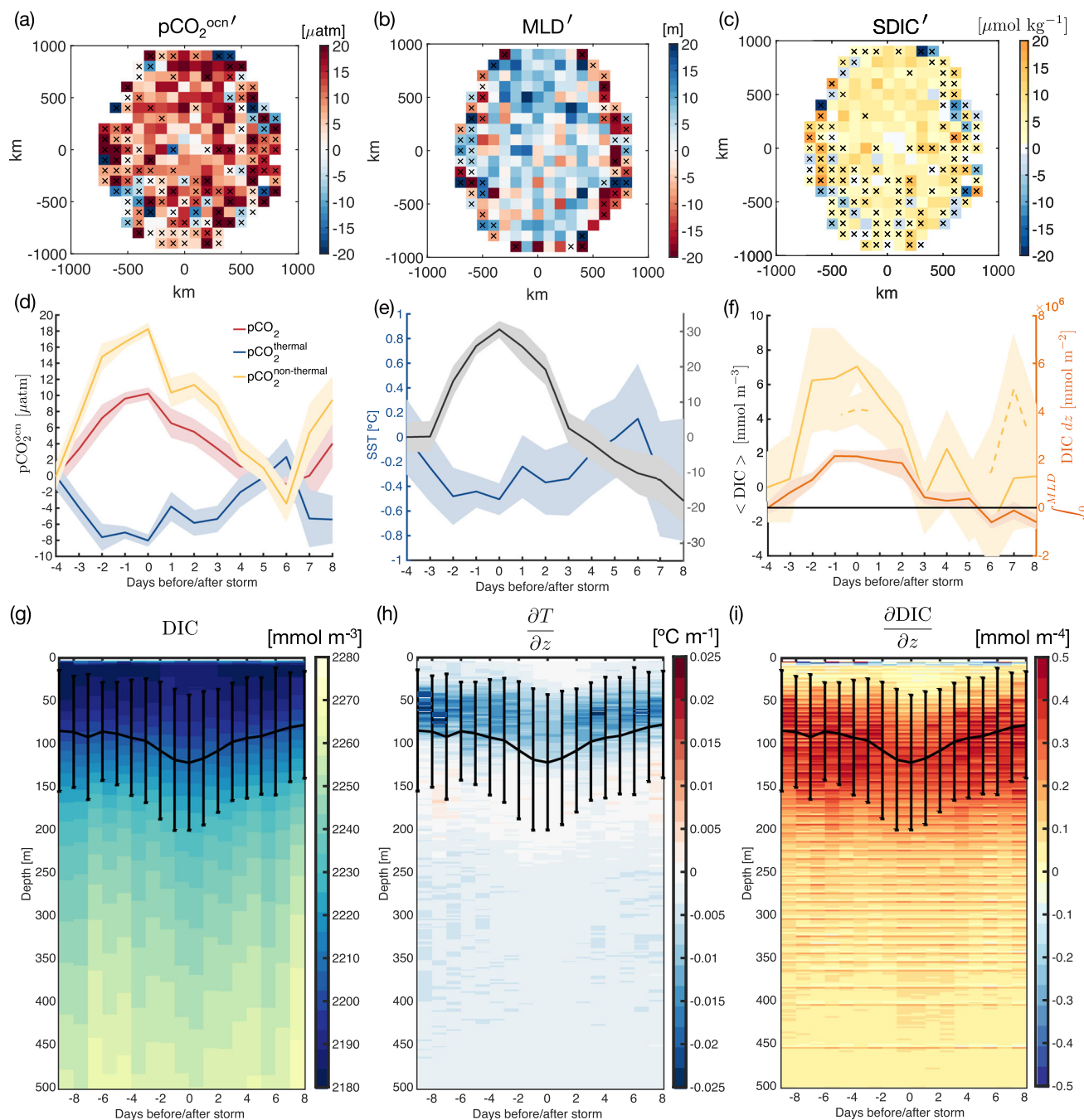


Fig. 6 | Storm anomalies derived from Argo float data, in storm-centric coordinates. Averaged surface (a) $p\text{CO}_2^{\text{ocn}'}$, b mixed-layer depth (MLD) and c surface DIC (SDIC) anomalies, for profile data within 1000 km of storm centers. d Surface $p\text{CO}_2^{\text{ocn}'}$ anomalies (red), and its decomposition into thermal (blue) and non-thermal components (yellow), e MLD (gray) and SST (blue) anomalies, anomalies for f surface DIC (solid yellow), MLD-averaged DIC (dashed yellow) and depth-integrated DIC to the base of the mixed layer (orange). g DIC profiles, h temperature and i DIC vertical gradients, as a function of days before/after storm passage. In the top panel, anomalies are calculated subtracting the monthly mean at the profile location from the SODA-ETHZ gridded product, whereas the middle and lower

panels show anomalies based entirely on float data (see Methods). Surface float data binned in $100\text{ km} \times 100\text{ km}$ where $N < 10$ observations are hatched. Spatially averaged $p\text{CO}_2^{\text{ocn}'}$ anomalies in a are $9.58 \pm 0.58\ \mu\text{atm}$, MLD anomalies in b are $4.06 \pm 0.75\ \text{m}$, and surface DIC anomalies in (c) are $4.83 \pm 0.30\ \mu\text{mol kg}^{-1}$. Note that storms are identified using SLP minima from ERA5 for the period 2014–2022 in the top panel; and as an event with averaged wind speed higher than $10\ \text{m s}^{-1}$ over the course of 3 days in the lower panels. Error bars represent the standard error for the mean, except in the lower panel, where error bars for the averaged MLD (solid black) represent one standard deviation.

in the model lag behind, showing their maximum surface expression ~5–7 days after the storm (Fig. 5c). We also note that storms seem to have a long-lasting effect in SST and surface DIC concentration anomalies, lasting > 30 days, implying surface heat fluxes are not restoring SST to pre-storm conditions as quickly as might have been expected from tropical cyclone studies³¹.

Float observations, on the other hand, suggest that the increase in $p\text{CO}_2^{\text{ocn}'}$ occurs within 1–2 days of a storm’s passage and it is driven by non-thermal effects (Fig. 6a, d). This is, while MLD deepening promotes sea surface cooling in the vicinity of a storm (Fig. 6b, e), and cooling, as expected, reduces $p\text{CO}_2^{\text{ocn}'}$ due to thermodynamic effects (Fig. 6d, blue line), non-thermal effects drive an increase in $p\text{CO}_2^{\text{ocn}'}$ by a larger magnitude, resulting

in an overall increase in $p\text{CO}_2^{\text{ocn}}$. Surface DIC anomalies derived from float data indicate an increase in DIC within the area of influence of a storm (Fig. 6c), as well as during the typical duration of a storm event (Fig. 6f), that is an order of magnitude larger compared to the model (Fig. 5). Altogether, the float data suggests entrainment of DIC from subsurface waters into the surface mixed layer, as the MLD deepens, as a candidate that drives ocean $p\text{CO}_2$ increases under a storm's influence. High-resolution observations indicate XLD deepening beyond the MLD can explain strong CO_2 outgassing events in the summer²⁴ more than changes in the MLD itself, but from float observations, we can only assess changes in MLD from hydrographic properties that are measured by the CTD sensor on the float.

The discrepancies in the temperature and DIC response between the model and observations can be in part attributed to the model's underestimation of MLD deepening after the passage of a storm. While there is MLD deepening in the model (Fig. 5a, b), the magnitude of the MLD anomalies is an order of magnitude less, compared to MLD anomalies under storm forcing in observations (i.e., $\mathcal{O}(10)$ m, Fig. 6b, e). Because the entrainment flux depends both on the entrainment velocity (i.e. due to MLD deepening), and the vertical gradient of temperature or DIC at the base of the mixed layer, it is also possible that the vertical gradients in the model are too weak or deeper in the water column. In Fig. 6g–i we show the averaged vertical structure for DIC, and vertical gradients for temperature and DIC as a function of time before/after a storm's passage, which indicate that these are enhanced near the base of the mixed layer.

Discussion

We described the role of storms in driving air-sea CO_2 flux in the Southern Ocean by means of a composite analysis in storm-centric coordinates, using a CESM ocean-ice integration as well as CO_2 fluxes derived from BGC Argo floats deployed in the Southern Ocean. There is a tendency of storms to induce CO_2 outgassing in a pattern that is slightly offset from the center of the low-pressure system, consistent with enhanced surface ocean mixing and cooling equatorward of storm centers. The temporal evolution of the air-sea CO_2 flux anomalies indicates strong outgassing anomalies collocated in time with the passage of a cyclone event. In the model, the dominant factor that drives the storm-induced air-sea CO_2 flux is the drop in atmospheric pressure that is used to compute $p\text{CO}_2$ in the atmosphere, while the response of ocean $p\text{CO}_2$ is relatively modest and the change in DIC out of phase with the strong outgassing signal. Air-sea CO_2 flux estimates derived from BGC Argo floats, show consistency in the sign of the storm CO_2 flux anomaly with the model, indicating outgassing. But the magnitude of the storm CO_2 flux anomaly is at least twice as large as in the model and there is a clear temporal signal in the CO_2 flux and $p\text{CO}_2^{\text{ocn}}$ anomaly associated with storms. Thus, observational estimates seem to suggest a stronger amplitude of ocean $p\text{CO}_2$ variability associated with storms than that indicated by the model.

Understanding why the model is unable to capture the increase in oceanic $p\text{CO}_2$ in storm conditions, and what drives the oceanic $p\text{CO}_2$ anomaly in observations requires further investigation and it is outside the scope of this study. There are some indications from Argo float observations that oceanic $p\text{CO}_2$ increases due to non-thermal effects, presumably driven by entrainment of DIC from subsurface waters (Fig. 6). Observations from a Waveglider-Glider mission in the Sub-Antarctic Zone also indicate that summer storm events able to induce CO_2 outgassing require that the mixing-layer penetrates deeper than the mixed-layer to produce entrainment of DIC²⁴. Entrainment of DIC appears to be one of the main drivers of strong synoptic variability in ocean $p\text{CO}_2$, along with horizontal Ekman advection driven by fluctuations in the westerly winds, in those observations. Entrainment of carbon-rich deep water has been identified as the dominant driver of carbon outgassing in float data on seasonal timescales, predominantly over the Indo-Pacific sector³⁷, where we find stronger storm CO_2 outgassing. It is possible that in this coarse resolution version of CESM mixing does not reach deep enough to entrain DIC from subsurface waters⁴¹, and/or that weak ventilation sets the DIC vertical gradient too deep. Weak ventilation and vertical exchange have been previously identified in CESM models on longer timescales^{42–44}. Additionally, changes in the

background diapycnal diffusivity can impact intra-annual air-sea CO_2 fluxes by altering the surface and vertical gradients of the carbonate system⁴⁵. As most ocean models use a time-invariant background diapycnal diffusivity, part of the discrepancy between CO_2 outgassing in CESM and BGC-Argo floats may be indicative of a more general discrepancy between modeled and observed impacts from storms on diffusivities.

Despite predominant CO_2 uptake in pre-storm conditions, Southern Ocean storms tend to induce outgassing, in contrast to what modelling studies of the CO_2 flux response to hurricanes have suggested in the subtropics³¹, where the high-winds (through the gas transfer coefficient) drive the CO_2 flux anomaly in the direction determined by the pre-existing $\Delta p\text{CO}_2$. A gas transfer parameterization more appropriate for high-wind conditions^{46,47} could lead to a larger storm CO_2 flux anomaly into the ocean due to the wind effect that overcompensates the anomaly driven by changes in $\Delta p\text{CO}_2$ (Fig. 4). However, a quadratic relationship between gas transfer and wind speed appears to be suitable for the Southern Ocean's high-wind conditions⁴⁸. We also note that for the float-based CO_2 flux estimates we use the same functional form of the gas transfer as in the model^{49,50}, and acknowledging changes in the wind speed product used could lead to large differences in the fluxes particularly in the Southern Ocean (~10%⁵¹), we employ the ERA5-derived coefficient for the piston velocity from Fay et al.⁵². An analogous CO_2 flux anomaly decomposition for float-based estimates indicates a larger contribution of the gas transfer coefficient (i.e., twice as large, Supplementary Fig. 7) compared to the model, but not yet large enough to overcompensate the $\Delta p\text{CO}_2$ -driven storm anomaly.

Unlike the case for hurricane-force tropical cyclones where changes in $p\text{CO}_2^{\text{ocn}}$ are typically $\mathcal{O}(10\text{--}100)$ μatm , changes in $p\text{CO}_2^{\text{ocn}}$ induced by Southern Hemisphere's storms are much more subtle ($\mathcal{O}(1\text{--}10)$ μatm , in observations) and comparable in magnitude to changes in $p\text{CO}_2^{\text{atm}}$ under storm forcing. This imposes a challenge for estimates of air-sea CO_2 fluxes in the Southern Ocean and assessments of driving mechanisms, as many factors can induce changes of comparable magnitudes in opposing directions.

Notably, the upper ocean response to the Southern Hemisphere's storms in CESM has a long-lasting effect on SST (and DIC) anomalies that do not recover pre-storm conditions even after several weeks. This is also different from what might be expected from tropical cyclone studies where SST anomalies recover to pre-storm conditions in a few weeks. The delayed SST cooling that peaks after several days is believed to be associated with the setup of a vortex-type circulation in the ocean around the cold core upwelling induced by the rotating winds and associated Ekman transport at the surface⁵³. As Son et al.⁵³ explain, the long-lasting effect of SST cooling is expected to persist longer in mid-latitudes due to the larger planetary vorticity. We also note that while tropical cyclones are summertime phenomena, SH's storms leave a stronger imprint on air-sea CO_2 fluxes in the wintertime, when heat fluxes into the ocean are expected to be weak (or rather out of the ocean^{54–56}). Thus, there is no restoring mechanism associated to radiative forcing and/or air-sea heat flux exchange to bring SSTs back to pre-storm conditions. Moreover, because of the coarse resolution of the ocean model, restratification processes, associated with baroclinic instabilities due to the formation of strong horizontal SST gradients, that could speed up the warming from the thermocline⁵⁷ would be suppressed.

Our estimate of the contribution of storms to the annual Southern Ocean's air-sea carbon exchange is within the range of estimates for storm's contributions to outgassing in the tropics (e.g., between +0.042 and +0.509 PgC yr^{-1} for tropical cyclones^{25,28}), and towards the lower bound of those estimates, as might be expected for relatively weaker cyclones in the extratropics. Despite large error bars in storm contributions to annual air-sea CO_2 exchange, our analysis suggests that the total contribution of storms to the air-sea CO_2 flux from the ocean to the atmosphere is an order of magnitude larger in float data, compared to the model, leading to 10–55% for floats vs. <10% for the model estimates (Fig. 3).

The estimate for the contribution of storms to the total Southern Ocean carbon flux from storm statistics in the model will be underestimated due to the coarse resolution of the model's atmospheric forcing, which lacks a good representation of the smaller mesoscale cyclones^{58,59}. However, accounting

for twice as many storms identified in ERA5 reanalysis relative to the CORE-IAF forcing (Supplementary Fig. 1) would result in an exchange of less than 0.1 PgC yr^{-1} in CESM, and only marginally within error bars but below the contribution estimated from float observations. We acknowledge the CESM model configuration may not be ideal for quantifying the storm's contributions to Southern Ocean carbon fluxes (e.g. no surface wave effects, coarse resolution ocean and forcing fields, daily coupling time interval with the atmosphere). A better representation of high-frequency processes in the ocean (e.g., associated with near-inertial waves), would enhance vertical mixing, the supply of carbon-rich waters to the surface, and CO_2 outgassing in the wintertime in an eddy-rich model of the Southern Ocean⁶⁰. Nonetheless, our results represent a first step towards assessing synoptic-scale storm influences on air-sea CO_2 exchange in the Southern Ocean, and are important in the context of model validation and structures of variability such as storms, which provide canonical phenomenology that Earth System Models should reproduce.

How will the Southern Ocean's carbon uptake change in a warming world given the expected trends in storm tracks, frequency and intensity of extratropical storms? The number of Southern Hemisphere's storms depends on the reanalysis datasets and tracking algorithms used^{61–63}, but differences in storm counts are less pronounced for the strongest storms. There is high confidence that the extratropical storms over the Southern Ocean have increased since the 1980's together with the observed poleward shift of the storm tracks^{62,64,65}. However, climate models tend to underestimate the intensity of extratropical storms due to their coarse horizontal resolution^{65,66} and are not able to reproduce the most intense mesoscale systems associated to polar lows or the rapid intensification of explosive cyclones^{67,68}. The main biases in the SH storm tracks persist in the latest generation of climate models (i.e., CMIP6), albeit some improvements presumably arise from improved model physics in the SH⁶⁹. Higher-resolution atmospheric models are needed to fully capture the extreme winds associated with explosive cyclones⁷⁰. Though projected increases in the intensity of SH storms remain somewhat uncertain^{71,72}, the projected southward shift of cyclonic activity can produce significant regional changes in extreme winds over the southern flank of the Antarctic Circumpolar Current (ACC). The southward shift and strengthening of the mean westerly winds has led to a weakening of the Southern Ocean carbon sink in the 1990's^{73–75}, due to natural CO_2 outgassing from changes in ocean circulation, and it is thought to be responsible for decadal variability in observations¹⁰. Quantifying the impact of storms on air-sea CO_2 fluxes is necessary to determine whether sampling alias might influence the inter-annual and decadal variability of the Southern Ocean carbon sink inferred from sparse shipboard data, from ships that typically avoid traversing through storms. We could speculate that strong CO_2 outgassing in response to an increase in SH storms would imply a weakening of the Southern Ocean carbon sink in future climate. However, given that our analysis indicates it is the CO_2 disequilibrium that drives the air-sea CO_2 exchange (as opposed to enhanced wind speeds), the atmospheric increase in CO_2 at a higher rate could imply a reduction in the $\Delta p\text{CO}_2$, and thus less storm CO_2 outgassing over time, which would rather strengthen the Southern Ocean as a carbon sink. More research is needed to assess trends of the role of storms for air-sea CO_2 exchange over the Southern Ocean.

A better understanding of present-day variations in air-sea CO_2 exchange in relation to physical forcing induced by storms is needed to better constrain future climate projections. Future studies aiming to find convergence of storm statistics and metrics (size, intensity, translation speed) in reanalysis products will be important to better assess storm controls on Southern Ocean air-sea CO_2 exchange, intra-seasonal as well as year-to-year variability. Despite large uncertainties in the magnitude of the storm CO_2 outgassing signal, we were able to demonstrate a basin-scale storm imprint in the upper ocean combining observations from Argo floats and surface winds. Thus, Argo floats, despite their coarse temporal sampling, by providing observations under all weather conditions, can collectively characterize event-scale phenomena such as storms on a basin scale. Storm CO_2 outgassing has the largest imprint in the wintertime when the

largest discrepancies in the strength of the Southern Ocean carbon sink between historical observations and float estimates have been detected^{18,19}. Wintertime shipboard observations, even if available, may not fully sample storm CO_2 outgassing events captured by the floats because ships will avoid crossings and/or turn off their underway systems in strong stormy conditions. Together with high-resolution observations from uncrewed vehicles and mooring sites, sustained BGC Argo observations are critical to further our understanding of the influence of storms on air-sea CO_2 exchange and other biogeochemical parameters relevant to ocean's health, and better constrain ocean models and future climate projections.

Methods

CESM Model

The ocean model is a hindcast run of the Parallel Ocean Program (POP, version 2) used to initialize the CESM (version 1) Decadal Prediction Large Ensemble (DPLE⁷⁶). It is a coarse resolution ocean, with a horizontal nominal grid spacing of $1^\circ \times 1^\circ$ where mesoscale eddies are parameterized by the Gent-McWilliams scheme⁷⁷. It has 60 vertical levels that increase in resolution from 250 m at depth to 10 m in the top 100 m. A branch simulation was run from Jan 1, 2009, onwards for 6 years saving 3D daily-averaged fields of physical and biogeochemical properties.

The ocean model is forced with the Coordinated Ocean-ice Reference Experiments (CORE) atmospheric dataset^{78,79}, which is based on NCEP/NCAR reanalysis products that have been adjusted with satellite data to correct global mean heat and freshwater fluxes. CORE winds are known to underestimate the wind intensity under tropical cyclones^{31,80}, and may as well be underestimated for the most intense extratropical storms of the Southern Hemisphere, but we have found relatively good agreement in storm's averaged winds between different reanalysis products (though the number of storms can differ significantly, Supplementary Note 1). CORE forcing includes 6-hourly SLP fields ($\sim 2^\circ$ horizontal resolution) that vary interannually (CORE Inter-Annually varying Forcing, CORE-IAF⁸¹). Because of the relatively coarse resolution of the atmospheric pressure fields, CORE does not capture mesoscale cyclones and underestimates the total number of storms (Supplementary Fig. 1). The coupling time interval between the forcing and ocean model is 1 day, implying the ocean sees daily averaged atmospheric fields. Thus, the ocean response in storm-centric coordinates represents an average over a day, when the storm occupied the region only a small fraction of that time (i.e., <15%, estimated from an average translation speed of $34.22 (\pm 4.99) \text{ km hr}^{-1}$ from storm tracks identified in CORE-IAF during the model run years). The coupling time interval may thus also result in an underestimation of the impact of weather systems on the ocean of CESM.

The biogeochemical and ecosystem model in CESM is of intermediate complexity (the Biogeochemical Elemental Cycling, BEC^{82,83}), with diagnostic equations for diatoms, small phytoplankton and diazotrophs, and one zooplankton. Phytoplankton's photo-adaptation strategies are accounted for by variable chlorophyll-a to carbon ratios⁸⁴, phytoplankton's growth can be limited by multiple nutrients (i.e., nitrate, ammonium, phosphate, silicate, and iron), and phytoplankton carbon losses include grazing, mortality, and aggregation. More details on the biogeochemical component of CESMv1 and validation analysis of mean patterns can be found in Krumhardt et al.⁸⁵ and other references^{44,86–88}. The ocean in CESMv1 is also coupled to a land model (the Community Land Model version 4, CLM4⁸⁹) and a sea-ice model (the Community Ice Code version 4, CICE4⁹⁰).

BGC Argo float data

We use float-derived carbon parameter estimates from profiling floats deployed by GO-BGC and SOCCOM^{16,91}, inferred from measured pH and total alkalinity estimated from the CARbonate system and Nutrients concentration from hYdrological properties and Oxygen using a Neural-network (CANYON-B) algorithm^{92,93}. We use the snapshot from April 2023 available from the GO-BGC and SOCCOM float data collection (at <https://library.ucsd.edu/dc/object/bb03521131>), and restrict the analysis to profile data collected between 2014 and 2022, when atmospheric CO_2 data are

available to compute fluxes. Details of the estimates of carbon parameters from the float's measured pH are in Williams et al.¹⁷ and Maurer et al.⁹⁴ and further discussed in the Supplementary. Surface values from float data (e.g., SST) and derived carbon parameters (surface DIC, and pCO₂) are averaged over the top 10 m.

Air-sea CO₂ fluxes in CESM

The air-sea CO₂ fluxes, F_{CO₂}, are parameterized as:

$$F_{CO_2} = k\alpha(1 - f_{ice}) \times \Delta pCO_2; \quad (2)$$

where the CO₂ gas transfer velocity k is calculated as a quadratic function of wind speed, w , α is the temperature- and salinity-dependent solubility coefficient for CO₂⁹⁵ and f_{ice} is the fraction of sea surface covered by ice. The gas transfer velocity is calculated as $k = a <w^2> \sqrt{(660/Sc)}$, where a is a proportionality constant and Sc is the temperature-dependent Schmidt number for CO₂, following Wanninkhof⁹⁹. Note that this version of the model uses the coefficient $a = 0.31$ in units of (cm h⁻¹) (m s⁻¹)⁻² from Wanninkhof⁴⁹.

ΔpCO_2 is the difference between partial pressures of CO₂ in the ocean, pCO₂^{ocn}, and atmosphere, pCO₂^{atm}, and is defined as:

$$\Delta pCO_2 = [pCO_2^{ocn} - pCO_2^{atm}]; \quad (3)$$

Thus, a positive F_{CO₂} flux indicates CO₂ out of the ocean, and a negative flux indicates CO₂ into the ocean. The partial pressure of CO₂ in the atmosphere is given by:

$$pCO_2^{atm} = X_{CO_2} \times p_{atm}; \quad (4)$$

where X_{CO_2} is the atmospheric mixing ratio of CO₂ (mol CO₂ per mol dry air), and p_{atm} the surface atmospheric pressure. A caveat for this forced-ocean model configuration is that X_{CO_2} is globally uniform and only varies annually⁹⁶, and thus local changes in pCO₂^{atm} are entirely driven by changes in p_{atm} . Nonetheless, sensitivity analysis of float-derived CO₂ fluxes using the global annual average X_{CO_2} from CESM forcing indicate that accounting for sub-annual variability in X_{CO_2} only slightly reduces storm CO₂ flux anomalies, and the discrepancy between the model and observational storm CO₂ outgassing magnitude is still robust (Supplementary Fig. 3d).

Air-sea CO₂ fluxes derived from Argo floats

The fluxes of CO₂ derived from float data are computed using the same flux parameterization as in the model (i.e., eq. (2)) but with the updated coefficient for the gas transfer velocity derived for ERA5 winds (Table 2 in Fay et al.⁵²).

We estimate pCO₂^{atm} for float data using the mole fraction of CO₂ in dry air from Cape Grim, and the collocated atmospheric surface pressure from ERA5 reanalysis⁹⁷ correcting for water vapor pressure⁹⁸:

$$pCO_2^{atm} = X_{CO_2} \times (p_{atm} - p_{H_2O}); \quad (5)$$

The water vapor pressure, p_{H_2O} , is calculated assuming that the air is 100% saturated with water vapor using the temperature and salinity dependence (see e.g., Appendix A1 in McGillis and Wanninkhof⁹⁹, from Weiss and Price¹⁰⁰). We note that the water vapor correction for pCO₂^{atm} is not accounted for in the model, but we apply this correction to estimate fluxes for float data for consistency with previous observational studies and baseline products. Not applying this correction for float data results in higher pCO₂^{atm}, a decrease in ΔpCO_2 , and thus, less outgassing.

To account for synoptic atmospheric variability in both the pCO₂^{atm} and gas transfer velocity coefficient, we collocated float's profile data with ERA5 reanalysis winds and surface atmospheric pressure (i.e., averaged within 6h, 12h, and 24h from a float's sampling time). We show results that use the daily averaged atmospheric state within a day of a float's sampling time. Note that for the calculation of $<w^2>$, we square the zonal and meridional components of the hourly winds and then average wind speeds

squared over the different periods to account for the fact that the average of the squares is larger than the square of the average.

The pCO₂^{ocn} is not directly measured by the floats but derived using measurements from pH sensors, as well as CTD and oxygen data to estimate total Alkalinity and carbon parameters^{91,94}. We acknowledge pCO₂^{ocn} inferred from float data may be biased high^{14,18,21,22,101-104}, and systematic biases could be potentially corrected by leveraging the higher accuracy O₂ data from the floats¹⁰². However, for the purpose of this study, we are interested in the change induced by storms relative to pre-storm conditions in a statistical sense (averaging across ~1000s of profiles). We test the sensitivity of the storm pCO₂^{ocn} anomalies to the empirical algorithm used to estimate Alkalinity and to the surface pH adjustment correction (see Supplementary Note 2).

Atmospheric reanalysis and satellite wind data

We use ERA5 reanalysis data^{97,105} to track storms and calculate air-sea CO₂ fluxes for float data (i.e., following Fay et al.⁵²). We extract the atmospheric state (i.e., hourly atmospheric surface pressure and 10-m wind vectors) for each profile, by collocating profiles to the closest ERA5 grid point in space (0.25° × 0.25°) and time (within a day). Near-surface winds (i.e., at 10-m height) are used to calculate the gas transfer velocity, and atmospheric pressure is used to calculate pCO₂^{atm}. We also use 6-hourly Mean Sea Level Pressure (SLP) fields from ERA5 for the identification and tracking of extratropical cyclones.

We also extract 10-m wind vectors from the Cross Calibrated Multi-Platform (CCMP¹⁰⁶) satellite product for the 10 days prior and post a float profile, and at the closest grid point (within 25 × 25 km of profile location) to composite float data in a before/after storm framework. ERA5 surface winds for the 10 days prior and post a float's profiling time are also extracted for sensitivity analysis of composite fields (Supplementary Fig. 7). Because CCMP winds are based on scatterometer winds which measure sea-surface roughness and are more intrinsically related to wind-stress, and showed smoothed and more consistent patterns than ERA5, we show results based on CCMP in the main text.

Atmospheric CO₂

We use monthly averaged air CO₂ from Cape Grim to compute pCO₂^{atm} because it allows us to extend the float data analysis up to December 2022. Air CO₂ from the NOAA Global View Marine Boundary Layer (MBL) observations, which vary latitudinally and weekly, as well as the annual global mean values from the CESM atmospheric forcing were also used for sensitivity analysis (Supplementary Note 3 and Supplementary Fig. 3d).

Sea ice

We use daily sea-ice concentration, on a 25 km × 25 km grid, from the NOAA's National Snow and Ice Data Center (NSIDC) Climate Data Record of Passive Microwave Sea Ice Concentration¹⁰⁷.

Storm identification, tracking and metrics

We track storms in the CORE-IAF forcing of the model using Tempest Extremes (TE), developed by Ullrich and Zarzycki¹⁰⁸. The algorithm identifies cyclones as SLP minima using closed contour criteria (i.e., as an increase in SLP of at least 200 Pa (2 hPa) within 4° of a candidate node). Storm tracks are constructed considering a maximum great circle distance of 8° between candidates, with a minimum of 8 candidate nodes per track and a maximum gap size of two (i.e., consecutive time steps with no associated candidate). For the analysis of BGC Argo float data, storms are identified in SLP fields from ERA5 reanalysis.

For sensitivity analysis, we also track storms in ERA5 using a different SLP-based algorithm^{63,109}, for the years 2011-2018. The storm-centric composite analysis using float data was repeated using the storms identified in CORE-IAF, showing qualitatively similar results. Comparisons of statistics for different storm characteristics (strength, frequency, duration, and size) for storms tracked in different forcing fields using the same algorithm (TE), and using different algorithms on the same reanalysis product (ERA5)

are presented in the Supplementary Note 1. Here we seek overall statistics for a typical storm, acknowledging each individual storm can deviate from the mean. We note that maximum winds within CORE-IAF and ERA5 storms are of comparable magnitude (on average, $\sim 21 \text{ m s}^{-1}$ with a standard deviation of 2.5 m s^{-1} , see Supplementary Table 1). However, due to its higher resolution the number of storms identified in ERA5 can double the number of storms in the CORE-IAF forcing each year. Thus, the contribution of storm outgassing to the annual Southern Ocean CO_2 exchange inferred from storm statistics in CESM could be twice as large if the forcing fields of the ocean model accounted for atmospheric mesoscale systems.

Storm anomalies

We calculate storm anomalies in CESM by subtracting from daily output fields the climatological daily mean for the 6-year run (period 2009–2014), and further remove any residual long-term variability by subtracting from the anomalies the averaged anomalies from the previous 10 days of a storm's passage around the area of impact (within 1000 km radius of a storm center). Storm composites are qualitative and quantitatively similar if we do not subtract a climatological daily mean first, but a small trend remains in the post-storm period, thus, for the model results we choose to subtract the climatological daily values (i.e., following Levy et al.³¹).

Because of the irregular sampling and spatial sparsity of BGC-Argo floats, not every storm is sampled by floats. For storms that are sampled by floats, there are at most 3 profiles within a storm. Thus we take a multi-step approach to accurately create observational storm composites. For float-based carbon parameters, we calculate storm anomalies by subtracting from each profile a fleet mean for profiles outside storms before compositing. We calculate a fleet mean outside storms for each month to account for seasonal variability in outside-storm conditions. Subtracting a mean flux outside storms by latitudinal bands ($30\text{--}50^\circ\text{S}$, and $50\text{--}90^\circ\text{S}$) in each ocean basin, to account for regional variability in outside-storm conditions, produces qualitatively similar results but float observations are not dense enough to distinguish a storm signal from noise for all subregions/months of the year (i.e., with $N < 100$, per month). This approach allows us to assess the storm anomaly entirely from float data and captures the outgassing enhanced equatorward of storm centers that we identify in the model (Fig. 1a), with comparable averaged CO_2 flux anomalies around storm centers, i.e. $1\text{--}1.45 \text{ mmol m}^{-2} \text{ day}^{-1}$, than if we were to compute anomalies relative to a baseline CO_2 flux product before compositing (Supplementary Notes 2 and 3). Note that mapped float-based CO_2 flux anomalies in Fig. 2b are relative to averaged fluxes from floats outside storms, but only $\sim 30\%$ of float fluxes shown in the map were sampled in the vicinity of a storm to be considered in the storm-centric average of Fig. 1c. For other variables with strong zonal gradients (such as SST or DIC), however, subtracting a fleet mean outside storms results in anomalies showing a zonal gradient in each latitudinal band/ocean basin. Thus, we considered subtracting a monthly mean (closest to the profile's sampling location) from available gridded products. Whenever possible, anomalies are calculated by subtracting the monthly mean closest to the profile date and location. We note that either approach results in anomalies of the same sign around storms, for any given variable, albeit of different magnitude.

Because we cannot subtract a mean value prior to a storm passage for each individual float profile, we acknowledge residual variability outside the atmospheric synoptic range (e.g. sub-monthly from the ocean mesoscale or inter-annual variability) may remain in anomalies for float data when collocated and averaged spatially around storm centers; but these would presumably average out in an overall storm-centric mean. In the time before/after storm passage framework, however, we are able to subtract the averaged pre-storm conditions (e.g., 4 days prior to the storm passage) in a statistical sense (i.e., after compositing and averaging variables in the time framework). We refer to storm anomalies, when referring to averaged anomalies in the vicinity of a cyclonic system in either the spatial or temporal domain, acknowledging the two approaches may convey different information in terms of the magnitude of storm anomalies.

The magnitude of storm anomalies could have different impacts depending on the local variability at the storm location. Thus, we also considered standardized anomalies dividing by the standard deviation of the seasonal cycle of the variable at each storm or profile location, before compositing. Standardized anomalies are unitless, or in standard units, and reduce the noise in the composite fields. We show standardized anomalies in monthly and latitudinally averaged CO_2 flux storm anomalies (Fig. 2c–d), and for storm composite fields of the fluxes in the Supplementary (Note 3).

Gridded carbon parameters and surface temperature

Storm anomalies derived from float data that are spatially collocated around storm centers (i.e., by identifying storms from SLP minima) are relative to a baseline mapped product, unless otherwise specified. Storm CO_2 flux anomalies relative to a baseline mapped product (i.e., analogous to Fig. 1c) are presented in the Supplementary Fig. 2.

As a baseline for pCO_2^{cn} we use the product from Landschutzer et al.¹¹⁰ (v2020), available from 1982 through December 2019 in a $1^\circ \times 1^\circ$ grid and monthly resolution. This product uses the Self-Organizing Map Feed-Forward Network (SOM-FFN) neural network to map sparse in situ observations of pCO_2^{cn} . For more details on the mapping technique and comparisons against other products, see Rodenbeck et al.¹¹¹. In the Supplementary, we show anomalies computed by subtracting smoothed pCO_2^{cn} monthly fields (i.e., from the nearest neighbor filter intended to filter out high-frequency variability associated to the ocean mesoscale¹¹⁰), but both the raw and smoothed pCO_2^{cn} monthly means produced qualitatively similar results (and a median difference of $0.13 \mu\text{atm}$ for the Southern Ocean). Note that the air-sea CO_2 flux calculation in Landschutzer et al.¹¹⁰ product uses a gas transfer velocity calculated from ERA5 reanalysis winds¹¹² and the CO_2 solubility constant is calculated from sea surface temperature¹¹³ and Hadley center EN4 sea surface salinity¹¹⁴ following Weiss⁹⁵. For CO_2 fluxes we use the SOM-FFN version available from the SeaFlux dataset⁵² because it provides updated estimates of the fluxes using atmospheric surface pressure from ERA5 and the re-scaled gas transfer coefficient for ERA5 winds.

As a baseline for DIC, we use monthly means from the Ocean SODA-ETHZ product¹¹⁵, available from 1985 through 2022 at a spatial resolution of $1^\circ \times 1^\circ$ (v2023). The Ocean SODA-ETHZ product also provides mapped ocean pCO_2 , which we also use to test the robustness of our results to the baseline product used to calculate anomalies (Supplementary, Table 2). SODA-ETHZ also provides mapped DIC, calculated from globally mapped pCO_2 and total Alkalinity from the Global Ocean Data Analysis Project (GLODAP¹¹⁶) using thermodynamic equations of the carbonate system (CO_2sys ¹¹⁷).

For sea surface temperature, we use the top 10 m of gridded monthly mean temperature fields from Roemmich and Gilson¹¹⁸, based on core Argo floats¹¹⁹. For MLD we use the monthly climatology constructed from core Argo float data by Holte et al.¹²⁰.

Compositing analysis

We extract tracer and anomaly fields from the model for the volume of water beneath each storm at all storm stages. We then construct averaged tracer anomalies across all storm realizations for surface fields, as well as meridional sections cutting across storms to look at storm imprints with depth (e.g., Fig. 5). Given the distinct imprint of air-sea CO_2 fluxes towards the equatorward side of storm centers in the model (Fig. 1a), to map storm imprints on air-sea CO_2 fluxes (Fig. 2a), we averaged spatially over the equatorward side of storms at every storm stage. To look at the evolution of the fields before and after a storm passage, we extract model output from 10-days-prior to 30-days-after a storm passed over a given area. For the averaged storm composite analysis, we only consider the storm stage at the maximum strength i.e., when the core SLP is at its minimum for a given storm track to avoid double counting storms (though each storm stage would have impacted a slightly different area as the storm moves eastward). Considering all storm stages (through a storm's life cycle) does not significantly modify results, making the extra compute time unnecessary.

Storm-centric composites of Argo float data are constructed by searching for float profile data within a 1000 km radius of each storm center. The great circle distance between the float's position and the storm center is calculated in km, and decomposed into dx and dy distances to remap float data in storm-centric coordinates (e.g., Fig. 1c). For the temporal evolution of Argo float data, before/after a storm passage, we extracted wind data within +/- 10 days of a float's profile. In this time-domain framework, a storm is identified as a high wind event using a wind speed threshold value of 10 m s⁻¹, with persistence over the course of 3 days. Considering the persistence of a wind event (i.e. 3-day averaged wind speed higher than the threshold) yields larger anomalies, as expected, but the details of the composite analysis beyond ± 3 days of a storm passage are sensitive to this choice, as well as the wind product used (CCMP vs ERA5, Supplementary Fig. 7). Thus, we only highlight results that were robust within a few days of a storm's passage.

Unless otherwise stated, the median is used as a metric for central value in composite analysis. We find median values tend to be smaller than the mean but show more coherent spatial patterns, whereas the mean can be subject to extreme responses (not necessarily in the direction of the median anomaly). To be conservative, when reporting the contribution of storm CO₂ fluxes we chose to use median values (and compare with the seasonal amplitude of the median CO₂ flux for the Southern Ocean). The use of standardized anomalies ameliorates noise in the anomalies (Supplementary Note 3), but we lose information on the size of anomalies in units of the variable.

CO₂ flux anomaly decomposition

To understand the source of variability in the storm CO₂ outgassing anomalies in the model, we perform a linear decomposition of anomalies of the air-sea CO₂ flux (i.e., a Taylor series expansion^{44,86}):

$$F'_{CO_2} \approx k'_w \times \overline{\Delta pCO_2} + \overline{k_w} \times (\Delta pCO_2)' + \dots \quad (6)$$

where the first term represents the contribution to the air-sea CO₂ flux from variations in the gas transfer velocity, solubility, and ice cover, and the second term arises from variability in the ΔpCO₂ anomalies. Note that cross terms in the decomposition are neglected, but the reconstruction of the total anomaly from these two terms explains a significant fraction of the variability in F'_{CO₂} (Fig. 4a, dashed and full black lines), suggesting cross terms have a negligible contribution, which is consistent with previous studies^{44,86}. Both the solubility and gas transfer velocity have a temperature dependence that cancels out, and thus, the first term predominantly reflects variability associated to changes in wind speed and ice cover⁸⁶.

Thermal vs non-thermal drivers of ocean pCO₂

To investigate the drivers of storm-induced changes in pCO₂^{ocn} from float data, we partition anomalies of pCO₂^{ocn} into components driven by thermodynamics effects (i.e., thermal) and non-thermal components^{121–124}:

$$pCO_2^{\text{thermal}} = \overline{pCO_2} \times \exp(\gamma_T * (SST - \overline{SST})) - \overline{pCO_2} \quad (7)$$

where γ_T = 0.0423 is the temperature sensitivity of CO₂. We perturbed the averaged pCO₂ for pre-storm conditions, $\overline{pCO_2}$, with the SST anomaly, SST - \overline{SST} , i.e. the difference between the SST within a storm and the averaged pre-storm or non-storm SST (depending on the framework of reference, see section on Compositing Analysis). Note that with float data, the analysis can only be done statistically, after compositing float data in a before/after storm framework. The non-thermal component is then calculated as a residual:

$$pCO_2^{\text{non-thermal}} = pCO_2^{\text{ocn}} - pCO_2^{\text{thermal}} \quad (8)$$

Data availability

CESM version 1 model code is available at <https://www.cesm.ucar.edu/models/cesm1.2/>. The DPLE hindcast run is available at <https://www.cesm.ucar.edu/projects/community-projects/DPLE/>. Daily integrated output

fields from the model run analyzed in this study are stored at NCAR's Geoscience Data Exchange (<https://gdex.ucar.edu/>, <https://doi.org/10.26024/hss6-m342>).

BGC Argo float data were collected and made freely available by the Southern Ocean Carbon and Climate Observations and Modeling (SOC-COM) Project funded by the National Science Foundation, Division of Polar Programs (NSF PLR-1425989), supplemented by NASA, and by the International Argo Program and the NOAA programs that contribute to it. GO-BGC and SOCCOM float data is accessible through the UCSD library at <https://library.ucsd.edu/dc/object/bb03521131>. The Argo Program is part of the Global Ocean Observing System. Core Argo data were collected and made freely available by the International Argo Program and the national programs that contribute to it (<http://www.argo.ucsd.edu>, <http://argo.jcommops.org>). The Argo Program is part of the Global Ocean Observing System.

ERA5 reanalysis data is produced by the European Centre for Medium-Range Weather Forecasts (ECMWF, <https://www.ecmwf.int/en/forecasts/dataset/ecmwf-reanalysis-v5>), and accessible in NetCDF format through the Research Data Archive at the National Center for Atmospheric Research, Computational and Information Systems Laboratory (<https://rda.ucar.edu/datasets/ds633.0/>). CCMP Version-2.0 vector wind analyses are produced by Remote Sensing Systems. Data are available at www.remss.com. NOAA Greenhouse Gas Marine Boundary Layer Reference data is available at <https://gml.noaa.gov/ccgg/mb/index.html>. Cape Grim Air Pollution station air CO₂ data can be accessed at <https://www.csiro.au/en/research/natural-environment/atmosphere/Latest-greenhouse-gas-data>. NOAA's National Snow and Ice data Center (NSIDC) Climate Data Record of Passive Microwave Sea Ice Concentration, Version 4 (G02202) are available at <https://nsidc.org/data/g02202/versions/4>. The SeaFlux dataset is available at <https://zenodo.org/record/5482547>.

Code availability

MATLAB code to generate the storm composite analysis and figures in this manuscript is available upon request.

Received: 9 May 2023; Accepted: 5 May 2024;

Published online: 21 May 2024

References

1. Sabine, C. L. et al. The oceanic sink for anthropogenic CO₂. *Science* **305**, 367–371 (2004).
2. Khatiwala, S., Primeau, F. & Hall, T. Reconstruction of the history of anthropogenic CO₂ concentrations in the ocean. *Nature* **462**, 346–349 (2010).
3. DeVries, T. The oceanic anthropogenic CO₂ sink: Storage, air-sea fluxes, and transports over the industrial era. *Glob. Biogeochem. Cycles* **28**, 631–647 (2014).
4. Frölicher, T. L. et al. Dominance of the Southern Ocean in anthropogenic carbon and heat uptake in CMIP5 models. *J. Clim.* **28**, 862–886 (2015).
5. Kessler, A. & Tjiputra, J. The Southern Ocean as a constraint to reduce uncertainty in future ocean carbon sinks. *Earth Syst. Dyn.* **7**, 295–312 (2016).
6. Anav, A. et al. Evaluating the land and ocean components of the global carbon cycle in the CMIP5 Earth System Models. *J. Clim.* **26**, 130401082723008 (2013).
7. Lenton, A. et al. Sea-air CO₂ fluxes in the southern ocean for the period 1990–2009. *Biogeosciences* **10**, 4037–4054 (2013).
8. Mongwe, N. P., Chang, N. & Monteiro, P. M. S. The seasonal cycle as a mode to diagnose biases in modelled CO₂ fluxes in the Southern Ocean. *Ocean Model.* **106**, 90–103 (2016).
9. Mongwe, N. P., Vichi, M. & Monteiro, P. M. S. The seasonal cycle of pCO₂ and CO₂ fluxes in the Southern Ocean: diagnosing anomalies in CMIP5 Earth system models. *Biogeosciences* **15**, 2851–2872 (2018).

10. Gruber, N., Landschützer, P. & Lovenduski, N. S. The variable Southern Ocean Carbon sink. *Annu. Rev. Mar. Sci.* **11**, 159–186 (2019).
11. Hauck, J. et al. Consistency and challenges in the ocean carbon sink estimate for the global carbon budget. *Front. Mar. Sci.* **7**, 571720 (2020).
12. Friedlingstein, P. et al. Global Carbon Budget 2022. *Earth Syst. Sci. Data* **14**, 4811–4900 (2022).
13. Monteiro, P., Gregor, L. & Levy, M. Intraseasonal variability linked to sampling alias in air-sea CO₂ fluxes in the Southern Ocean. *Geophys. Res. Lett.* **42**, 8507–8514 (2015).
14. Sutton, A. J., Williams, N. L. & Tilbrook, B. Constraining Southern Ocean CO₂ flux uncertainty using uncrewed surface vehicle observations. *Geophys. Res. Lett.* **48**, e2020GL091748 (2021).
15. Djeutchouang, L. M., Chang, N., Gregor, L., Vichi, M. & Monteiro, P. M. S. The sensitivity of pCO₂ reconstructions to sampling scales across a Southern Ocean sub-domain: a semi-idealized ocean sampling simulation approach. *Biogeosciences* **19**, 4171–4195 (2022).
16. Johnson, K. S. et al. Biogeochemical sensor performance in the SOCCOM profiling float array. *J. Geophys. Res. Oceans* **122**, 6416–6436 (2017).
17. Williams, N. L. et al. Calculating surface ocean pCO₂ from biogeochemical Argo floats equipped with pH: An uncertainty analysis. *Glob. Biogeochem. Cycles* **31**, 591–604 (2017).
18. Gray, A. R. et al. Autonomous biogeochemical floats detect significant carbon dioxide outgassing in the high-latitude Southern Ocean. *Geophys. Res. Lett.* **45**, 9049–9057 (2018).
19. Bushinsky, S. M. et al. Reassessing Southern Ocean air-sea CO₂ Flux estimates with the addition of biogeochemical float observations. *Glob. Biogeochem. Cycles* **33**, 1370–1388 (2019).
20. Gray, A. R. The four-dimensional carbon cycle of the southern ocean. *Annu. Rev. Mar. Sci.* **16**, null (2024).
21. Long, M. C. et al. Strong Southern Ocean carbon uptake evident in airborne observations. *Science* **374**, 1275–1280 (2021).
22. Mackay, N. & Watson, A. Winter Air-Sea CO₂ fluxes constructed from summer observations of the polar Southern Ocean suggest weak outgassing. *J. Geophys. Res. Oceans* **126**, e2020JC016600 (2021).
23. Sabine, C. L. et al. Evaluation of a new carbon dioxide system for autonomous surface vehicles. *J. Atmos. Ocean. Technol.* **37**, 1305–1317 (2020).
24. Nicholson, S.-A. et al. Storms drive outgassing of CO₂ in the subpolar Southern Ocean. *Nat. Commun.* **13**, 158 (2022).
25. Bates, N. R., Knap, A. H. & Michaels, A. F. Contribution of hurricanes to local and global estimates of air-sea exchange of CO₂. *Nature* **395**, 1–4 (1998).
26. Nemoto, K. et al. Continuous observations of atmospheric and oceanic CO₂ using a moored buoy in the East China Sea: Variations during the passage of typhoons. *Deep Sea Res. Part II* **56**, 542–553 (2009).
27. Ye, H. et al. Variation of pCO₂ concentrations induced by tropical cyclones “Wind-Pump” in the middle-latitude surface oceans: A comparative study. *PLoS One* **15**, e0226189 (2020).
28. Huang, P. & Imberger, J. Variation of pCO₂ in ocean surface water in response to the passage of a hurricane. *J. Geophys. Res. Oceans* **115**, C10024 (2010).
29. Ko, Y. H., Park, G.-H., Kim, D. & Kim, T.-W. Variations in Seawater pCO₂ associated with vertical mixing during tropical cyclone season in the Northwestern Subtropical Pacific Ocean. *Front. Mar. Sci.* **8**, 679314 (2021).
30. Yu, P. et al. Effects of Typhoons on surface seawater pCO₂ and Air-sea CO₂ fluxes in the Northern South China Sea. *J. Geophys. Res. Oceans* **125**, e2020JC016258 (2020).
31. Levy, M. et al. Contribution of tropical cyclones to the air-sea CO₂ flux: A global view. *Glob. Biogeochem. Cycles* **26**, GB2001 (2012).
32. Fung, I., Prentice, K., Matthews, E., Lerner, J. & Russell, G. Three-dimensional tracer model study of atmospheric CO₂: Response to seasonal exchanges with the terrestrial biosphere. *J. Geophys. Res. Oceans* **88**, 1281–1294 (1983).
33. Parazoo, N. C. et al. Moist synoptic transport of CO₂ along the mid-latitude storm track. *Geophys. Res. Lett.* **38** (9) (2011).
34. Thilakan, V. et al. Towards monitoring the CO₂ source-sink distribution over India via inverse modelling: quantifying the fine-scale spatiotemporal variability in the atmospheric CO₂ mole fraction. *Atmos. Chem. Phys.* **22**, 15287–15312 (2022).
35. Carranza, M. M. et al. When mixed layers are not mixed. Storm-driven mixing and bio-optical vertical gradients in mixed layers of the Southern Ocean. *J. Geophys. Res.* **123**, 7264–7289 (2018).
36. Sarmiento, J. L. et al. The Southern Ocean Carbon and Climate Observations and Modeling (SOCCOM) project: A review. *Prog. Oceanogr.* **219**, 103130 (2023).
37. Prend, C. J. et al. Indo-Pacific Sector dominates Southern Ocean Carbon outgassing. *Glob. Biogeochem. Cycles* **36**, e2021GB007226 (2022).
38. Price, J. Upper Ocean response to a hurricane. *J. Phys. Oceanogr.* **11**, 153–175 (1981).
39. Jacob, S. D., Shay, L. K., Mariano, A. J. & Black, P. G. The 3D Oceanic mixed layer response to hurricane Gilbert. *J. Phys. Oceanogr.* **30**, 1407–1429 (2000).
40. D’Asaro, E. A. The ocean boundary layer below Hurricane Dennis. *J. Phys. Oceanogr.* **33**, 561–579 (2003).
41. DuVivier, A. K., Large, W. G. & Small, R. J. Argo observations of the deep mixing band in the Southern Ocean: A salinity modeling challenge. *J. Geophys. Res. Oceans* **123**, 7599–7617 (2018).
42. Thornton, P. E. et al. Carbon-nitrogen interactions regulate climate-carbon cycle feedbacks: results from an atmosphere-ocean general circulation model. *Biogeosciences* **6**, 2099–2120 (2009).
43. Wang, S., Moore, J. K., Primeau, F. W. & Khatiwala, S. Simulation of anthropogenic CO₂ uptake in the CCSM3.1 ocean circulation-biogeochemical model: comparison with data-based estimates. *Biogeosciences* **9**, 1321–1336 (2012).
44. Long, M. C., Lindsay, K., Peacock, S., Moore, J. K. & Doney, S. C. Twentieth-century oceanic carbon uptake and storage in CESM1(BGC)*. *J. Clim.* **26**, 6775–6800 (2013).
45. Ellison, E., Mashayek, A. & Mazloff, M. The sensitivity of southern ocean air-sea carbon fluxes to background turbulent diapycnal mixing variability. *J. Geophys. Res. Oceans* **128**, e2023JC019756 (2023).
46. Perrie, W., Zhang, W., Ren, X., Long, Z. & Hare, J. The role of midlatitude storms on air-sea exchange of CO₂. *Geophys. Res. Lett.* **31**, L09306 (2004).
47. Hare, J. E. et al. Evaluation of the National Oceanic and Atmospheric Administration/Coupled-Ocean Atmospheric Response Experiment (NOAA/COARE) air-sea gas transfer parameterization using GasEx data. *J. Geophys. Res.* **109**, C08S11 (2004).
48. Ho, D. T. et al. Measurements of air-sea gas exchange at high wind speeds in the Southern Ocean: Implications for global parameterizations. *Geophys. Res. Lett.* **33**, L16611 (2006).
49. Wanninkhof, R. Relationship between wind speed and gas exchange over the ocean. *J. Geophys. Res. Oceans* **97**, 7373–7382 (1992).
50. Wanninkhof, R. Relationship between wind speed and gas exchange over the ocean revisited. *Limnol. Oceanogr. Methods* **12**, 351–362 (2014).
51. Roobaert, A., Laruelle, G. G., Landschützer, P. & Regnier, P. Uncertainty in the global oceanic CO₂ uptake induced by wind forcing: quantification and spatial analysis. *Biogeosciences* **15**, 1701–1720 (2018).
52. Fay, A. R. et al. SeaFlux: harmonization of air-sea CO₂ fluxes from surface pCO₂ data products using a standardized approach. *Earth Syst. Sci. Data* **13**, 4693–4710 (2021).

53. Son, J.-H., Heo, K.-Y., Choi, J.-W. & Kwon, J.-i Long-lasting upper ocean temperature responses induced by intense typhoons in mid-latitude. *Sci. Rep.* **12**, 5752 (2022).
54. Dong, S., Gille, S. T. & Sprintall, J. An Assessment of the Southern Ocean mixed layer heat budget. *J. Clim.* **20**, 4425–4442 (2007).
55. Cerovečki, I., Talley, L. D. & Mazloff, M. R. A comparison of Southern Ocean air-sea buoyancy flux from an ocean state estimate with five other products. *J. Clim.* **24**, 6283–6306 (2011).
56. Ogle, S. E. et al. Episodic Southern Ocean heat loss and its mixed layer impacts revealed by the farthest south multiyear surface flux mooring. *Geophys. Res. Lett.* **45**, 5002–5010 (2018).
57. Mei, W. & Pasquero, C. Restratification of the upper ocean after the passage of a tropical cyclone: a numerical study. *J. Phys. Oceanogr.* **42**, 1377–1401 (2012).
58. Condron, A., Bigg, G. R. & Renfrew, I. A. Polar mesoscale cyclones in the Northeast Atlantic: Comparing Climatologies from ERA-40 and Satellite Imagery. *Mon. Wea. Rev.* **134**, 1518–1533 (2006).
59. Irving, D., Simmonds, I. & Keay, K. Mesoscale cyclone activity over the ice-free Southern Ocean: 1999–2008. *J. Clim.* **23**, 5404–5420 (2010).
60. Song, H., Marshall, J., Campin, J. & McGillicuddy, D. J. Impact of near-inertial waves on vertical mixing and air-sea CO₂ fluxes in the Southern Ocean. *J. Geophys. Res. Oceans* **124**, 4605–4617 (2019).
61. Neu, U. et al. IMILAST A community effort to intercompare extratropical cyclone detection and tracking algorithms. *BAMS* **94**, 529–547 (2013).
62. Wang, X. L., Feng, Y., Chan, R. & Isaac, V. Inter-comparison of extratropical cyclone activity in nine reanalysis datasets. *Atmos. Res.* **181**, 133–153 (2016).
63. Di Luca, A., Evans, J. P., Pepler, A., Alexander, L. & Argüeso, D. Resolution sensitivity of cyclone climatology over Eastern Australia using six reanalysis products*. *J. Clim.* **28**, 9530–9549 (2015).
64. Reboita, M. S., Rocha, R. P. D., Ambrizzi, T. & Gouveia, C. D. Trend and teleconnection patterns in the climatology of extratropical cyclones over the Southern Hemisphere. *Clim. Dyn.* **45**, 1929–1944 (2015).
65. Seneviratne, S. et al. *Weather and Climate Extreme Events in a Changing Climate*, 1513–1766 (Cambridge University Press, Cambridge, United Kingdom and New York, NY, USA, 2021).
66. Di Luca, A., Evans, J. P., Pepler, A. S., Alexander, L. V. & Argüeso, D. Evaluating the representation of Australian East Coast Lows in a regional climate model ensemble. *J. South. Hemisph. Earth Syst. Sci.* **66**, 108–124 (2016).
67. Haarsma, R. J. et al. High Resolution Model Intercomparison Project (HighResMIP v1.0) for CMIP6. *Geosci. Model Dev.* **9**, 4185–4208 (2016).
68. Moreno-Ibáñez, M., Laprise, R. & Gachon, P. Recent advances in polar low research: Current knowledge, challenges and future perspectives. *Tellus A: Dyn. Meteorol. Oceanogr.* **73**, 1–31 (2021).
69. Priestley, M. D. K. et al. An overview of the extratropical storm tracks in CMIP6 historical simulations an overview of the extratropical storm tracks in CMIP6 historical simulations. *J. Clim.* **33**, 6315–6343 (2020).
70. Jiayang, G. et al. Influence of model resolution on bomb cyclones revealed by HighResMIP-PRIMAVERA simulations. *Environ. Res. Lett.* **15**, 084001 (2020).
71. Chang, E. K. M. Projected significant increase in the number of extreme extratropical cyclones in the Southern Hemisphere. *J. Clim.* **30**, 4915–4935 (2017).
72. Yettella, V. & Kay, J. E. How will precipitation change in extratropical cyclones as the planet warms? Insights from a large initial condition climate model ensemble. *Clim. Dyn.* **49**, 1765–1781 (2017).
73. Le Quéré, C. et al. Saturation of the Southern Ocean CO₂ sink due to recent climate change. *Science* **316**, 1735–1738 (2007).
74. Lenton, A. & Matear, R. J. Role of the Southern Annular Mode (SAM) in Southern Ocean CO₂ uptake. *Glob. Biogeochem. Cycles* **21**, GB2016 (2007).
75. Lovenduski, N. S., Gruber, N. & Doney, S. C. Toward a mechanistic understanding of the decadal trends in the Southern Ocean carbon sink. *Glob. Biogeochem. Cycles* **22**, GB3016 (2008).
76. Yeager, S. G. et al. Predicting near-term changes in the earth system: a large ensemble of initialized decadal prediction simulations using the community earth system model. *Bull. Am. Meteorol. Soc.* **99**, 1867–1886 (2018).
77. Gent, P. R. & McWilliams, J. C. Isopycnal Mixing in Ocean Circulation Models. *J. Phys. Oceanogr.* **20**, 150–155 (1990).
78. Griffies, S. M. et al. Ocean modelling. *Ocean Model.* **26**, 1–46 (2009).
79. Large, W. G. & Yeager, S. G. The global climatology of an interannually varying air-sea flux data set. *Clim. Dyn.* **33**, 341–364 (2009).
80. Menkes, C. E. et al. Global impact of tropical cyclones on primary production. *Glob. Biogeochem. Cycles* **30**, 767–786 (2016).
81. Large, W. G. & Yeager, S. G. The global climatology of an interannually varying air-sea flux data set. *Clim. Dyn.* **33**, 341–364 (2008).
82. Moore, J. K., Doney, S. C. & Lindsay, K. Upper ocean ecosystem dynamics and iron cycling in a global three-dimensional model. *Glob. Biogeochem. Cycles* **18**, GB4028 (2004).
83. Moore, J. K., Lindsay, K., Doney, S. C., Long, M. C. & Misumi, K. Marine Ecosystem Dynamics And Biogeochemical Cycling In The Community Earth System Model [CESM1(BGC)]: Comparison of the 1990s with the 2090s under the RCP4.5 and RCP8.5 Scenarios. *J. Clim.* **26**, 9291–9312 (2013).
84. Geider, R. J., MacIntyre, H. L. & Kana, T. M. A dynamic regulatory model of phytoplankton acclimation to light, nutrients, and temperature. *Limnol. Oceanogr.* **43**, 679–694 (1998).
85. Krumhardt, K. M., Long, M. C., Sylvester, Z. T. & Petrik, C. M. Climate drivers of Southern Ocean phytoplankton community composition and potential impacts on higher trophic levels. *Front. Mar. Sci.* **9**, 916140 (2022).
86. Doney, S. C. et al. Skill metrics for confronting global upper ocean ecosystem-biogeochemistry models against field and remote sensing data. *J. Mar. Syst.* **76**, 95–112 (2009).
87. Lima, I. D., Lam, P. J. & Doney, S. C. Dynamics of particulate organic carbon flux in a global ocean model. *Biogeosciences* **11**, 1177–1198 (2014).
88. Krumhardt, K. M., Lovenduski, N. S., Long, M. C. & Lindsay, K. Avoidable impacts of ocean warming on marine primary production: Insights from the CESM ensembles. *Glob. Biogeochem. Cycles* **31**, 114–133 (2017).
89. Lawrence, P. J. et al. Simulating the biogeochemical and biogeophysical impacts of transient land cover change and wood harvest in the Community Climate System Model (CCSM4) from 1850 to 2100. *J. Clim.* **25**, 3071–3095 (2012).
90. Hunke, E. C. & Lipscomb, W. H. CICE: the Los Alamos Sea Ice Model Documentation and Software User's Manual Version 4.0. Tech. Rep., Los Alamos National Laboratory (2010).
91. Johnson, K. S. et al. SOCCOM float data - snapshot 2021-05-05. In Southern Ocean carbon and climate observations and modeling (SOCCOM) float data archive. (2021). UC San Diego Library Digital Collections.
92. Sauzède, R. et al. Estimates of water-column nutrient concentrations and carbonate system parameters in the global ocean: a novel approach based on neural networks. *Front. Mar. Sci.* **4**, 128 (2017).
93. Bittig, H. C. et al. An alternative to static climatologies: robust estimation of open ocean CO₂ variables and nutrient concentrations from T, S, and O₂ data using Bayesian neural networks. *Front. Mar. Sci.* **5**, 328 (2018).
94. Maurer, T. L., Plant, J. N. & Johnson, K. S. Delayed-mode quality control of oxygen, nitrate, and pH data on SOCCOM biogeochemical profiling floats. *Front. Mar. Sci.* **8**, 683207 (2021).
95. Weiss, R. Carbon dioxide in water and seawater: the solubility of a non-ideal gas. *Mar. Chem.* **2**, 203–215 (1974).

96. Meinshausen, M. et al. The RCP greenhouse gas concentrations and their extensions from 1765 to 2300. *Clim. Change* **109**, 213 (2011).
97. Hersbach, H. et al. The ERA5 global reanalysis. *Quart. J. Roy. Meteorol. Soc.* **146**, 1999–2049 (2020).
98. Dickson, A.G., Sabine, C.L. and Christian, J.R. (Eds.) Guide to best practices for ocean CO₂ measurements. PICES Special Publication 3, 191 pp. (2007).
99. McGillis, W. R. & Wanninkhof, R. Aqueous CO₂ gradients for air–sea flux estimates. *Mar. Chem.* **98**, 100–108 (2006).
100. Weiss, R. & Price, B. Nitrous oxide solubility in water and seawater. *Mar. Chem.* **8**, 347–359 (1980).
101. Fay, A. R. et al. Utilizing the Drake Passage Time-series to understand variability and change in subpolar Southern Ocean pCO₂. *Biogeosciences* **15**, 3841–3855 (2018).
102. Wu, Y. et al. Integrated analysis of carbon dioxide and oxygen concentrations as a quality control of ocean float data. *Commun. Earth Environ.* **3**, 92 (2022).
103. Bushinsky, S. M. & Cerovečki, I. Subantarctic mode water biogeochemical formation properties and interannual variability. *AGU Adv.* **4**, e2022AV000722 (2023).
104. Coggins, A. et al. Surface ocean carbon budget in the 2017 South Georgia diatom bloom: Observations and validation of profiling biogeochemical Argo floats. *Deep Sea Res. Part II* **209**, 105275 (2023).
105. European Centre for Medium-Range Weather Forecasts. 2019, updated monthly. ERA5 Reanalysis (0.25 Degree Latitude-Longitude Grid). Research Data Archive at the National Center for Atmospheric Research, Computational and Information Systems Laboratory. <https://doi.org/10.5065/BH6N-5N20>. Accessed† 22 Nov 2022.
106. Atlas, R. et al. A cross-calibrated, multiplatform ocean surface wind velocity product for meteorological and oceanographic applications. *Bull. Am. Meteorol. Soc.* **92**, 157–174 (2011).
107. Meier, W. N., F. Fetterer, A. K. Windnagel, and J. S. Stewart. NOAA/NSIDC Climate Data Record of Passive Microwave Sea Ice Concentration, Version 4 [G02202]. Boulder, Colorado USA. National Snow and Ice Data Center. <https://doi.org/10.7265/efmz-2t65>. Date Accessed 11-17-2022. (2021)
108. Ullrich, P. A. & Zarzycki, C. M. TempestExtremes: a framework for scale-insensitive pointwise feature tracking on unstructured grids. *Geosci. Model Dev.* **10**, 1069–1090 (2017).
109. Pepler, A. S., Di Luca, A. & Evans, J. P. Independently assessing the representation of midlatitude cyclones in high-resolution reanalyses using satellite observed winds. *Int. J. Climatol.* **38**, 1314–1327 (2017).
110. Landschützer, P., Gruber, N. & Bakker, D. C. E. An observation-based global monthly gridded sea surface pCO₂ product from 1982 onward and its monthly climatology (NCEI accession 0160558). version 5.5. (2020).
111. Rödenbeck, C. et al. Data-based estimates of the ocean carbon sink variability - first results of the Surface Ocean pCO₂ Mapping intercomparison (SOCOM). *Biogeosciences* **12**, 7251–7278 (2015).
112. Hersbach, H. et al. Complete ERA5 from 1940: Fifth generation of ECMWF atmospheric reanalyses of the global climate. Copernicus Climate Change Service (C3S) Data Store (CDS) (2017). <https://doi.org/10.24381/cds.143582cf>
113. Reynolds, R. W., Rayner, N. A., Smith, T. M., Stokes, D. C. & Wang, W. An improved in situ and satellite SST analysis for climate. *J. Clim.* **15**, 1609–1625 (2002).
114. Good, S. A., Martin, M. J. & Rayner, N. A. EN4: Quality controlled ocean temperature and salinity profiles and monthly objective analyses with uncertainty estimates. *J. Geophys. Res. Oceans* **118**, 6704–6716 (2013).
115. Gregor, L. & Gruber, N. OceanSODA-ETHZ: a global gridded data set of the surface ocean carbonate system for seasonal to decadal studies of ocean acidification. *Earth Syst. Sci. Data* **13**, 777–808 (2021).
116. Olsen, A. et al. Glodapv2.2019 – an update of glodapv2. *Earth Syst. Sci. Data* **11**, 1437–1461 (2019).
117. Lewis, E., Wallace, D. & Allison, L. J. Program developed for CO₂ system calculations. United States: N. p. Web. <https://doi.org/10.2172/639712> (1998).
118. Roemmich, D. & Gilson, J. The 2004–2008 mean and annual cycle of temperature, salinity, and steric height in the global ocean from the Argo Program. *Prog. Oceanogr.* **82**, 81–100 (2009).
119. Argo. Argo float data and metadata from Global Data Assembly Centre (Argo GDAC). (SEANOE, 2022). <https://doi.org/10.17882/42182>
120. Holte, J., Talley, L. D., Gilson, J. & Roemmich, D. An Argo mixed layer climatology and database. *Geophys. Res. Lett.* **44**, 5618–5626 (2017).
121. Takahashi, T., Olafsson, J., Goddard, J. G., Chipman, D. W. & Sutherland, S. C. Seasonal variation of CO₂ and nutrients in the high-latitude surface oceans: A comparative study. *Glob. Biogeochem. Cycles* **7**, 843–878 (1993).
122. Landschützer, P., Gruber, N., Bakker, D. C. E., Stemmler, I. & Six, K. D. Strengthening seasonal marine CO₂ variations due to increasing atmospheric CO₂. *Nat. Clim. Change* **8**, 146–150 (2018).
123. Nickford, S. et al. Autonomous Wintertime observations of air–sea exchange in the gulf stream reveal a perfect storm for ocean CO₂ Uptake. *Geophys. Res. Lett.* **49**, e2021GL096805 (2022).
124. Wanninkhof, R., Pierrot, D., Sullivan, K., Mears, P. & Barbero, L. Comparison of discrete and underway CO₂ measurements: Inferences on the temperature dependence of the fugacity of CO₂ in seawater. *Mar. Chem.* **247**, 104178 (2022).

Acknowledgements

M.M.C. was funded by the Advance Study Program (ASP) at NCAR and the MBARI Postdoctoral Fellowships during the course of this research. This work was sponsored by NSF’s Southern Ocean Carbon and Climate Observations and Modeling (SOCCOM) Project under the NSF Awards PLR-1425989 and OPP-1936222, with additional support from NOAA and NASA. Logistical support for this project in the Antarctic was provided by the U.S. National Science Foundation through the U.S. Antarctic Program. A.J.F. was supported by NOAA’s Pacific Marine Environmental Laboratory. This is PMEL contribution 5503. We thank the Ocean Section in Global Climate Dynamics (CGD), in particular Steve Yeager, Keith Lindsay, and Michael Levy for assistance with the model run. Colin Zarzycki for the development and assistance with the cyclone tracking code on NCAR’s computing system.

Author contributions

M.M.C. and M.C.L. conceived the study. M.M.C. undertook the analysis and drafted the manuscript. A.D.L. and K.E.T. performed the ERA5 storm identification and tracking. M.C.L. guided the examination of CO₂ flux drivers. N.P.M. contributed to model validation analysis. Y.T. contributed with float-based pCO₂ estimates for sensitivity analysis. A.J.F., K.S.J. and Y.T. provided guidance on float-based CO₂ flux estimates and analysis.

Competing interests

The authors declare no competing interests.

Additional information

Supplementary information The online version contains supplementary material available at <https://doi.org/10.1038/s41612-024-00657-7>.

Correspondence and requests for materials should be addressed to Magdalena M. Carranza.

Reprints and permissions information is available at <http://www.nature.com/reprints>

Publisher's note Springer Nature remains neutral with regard to jurisdictional claims in published maps and institutional affiliations.

Open Access This article is licensed under a Creative Commons Attribution 4.0 International License, which permits use, sharing, adaptation, distribution and reproduction in any medium or format, as long as you give appropriate credit to the original author(s) and the source, provide a link to the Creative Commons licence, and indicate if changes were made. The images or other third party material in this article are included in the article's Creative Commons licence, unless indicated otherwise in a credit line to the material. If material is not included in the article's Creative Commons licence and your intended use is not permitted by statutory regulation or exceeds the permitted use, you will need to obtain permission directly from the copyright holder. To view a copy of this licence, visit <http://creativecommons.org/licenses/by/4.0/>.

© The Author(s) 2024